Mixing of a conserved scalar in a turbulent reacting shear layer

By C. PANTANO†, S. SARKAR‡ AND F. A. WILLIAMS

Department of Mechanical and Aerospace Engineering, University of California San Diego,
9500 Gilman Drive, La Jolla CA 92093-0411, USA

Mixing of a conserved scalar representing the mixture fraction, of primary importance in modelling non-premixed turbulent combustion, is studied by direct numerical simulation (DNS) in strongly turbulent planar shear layers both with and without heat release at a reaction sheet. For high heat release, typical of hydrocarbon combustion, the mixing is found to be substantially different than without heat release. The probability density function of the scalar and the conditional rate of scalar dissipation are affected by the heat release in such a way that the heat release substantially decreases the overall reaction rate. To help clarify implications of the assumptions underlying popular models for interaction between turbulence and chemistry, the local structure of the scalar dissipation rate at the reaction sheet is extracted from the DNS database. The applicability of flamelet models for the rate of scalar dissipation is examined. To assist in modelling, a characteristic length scale is defined, representing the distance around the reaction sheet over which the scalar field is locally linear, and statistical properties of this length scale are investigated. This length scale can be used in studying values of the rate of scalar dissipation that mark the boundary between flames that feel a constant scalar dissipation field and those that do not.

1. Introduction

A common approach in the modelling of non-premixed turbulent combustion is based on knowledge of two variables: a mixture fraction, Z, that represents the mixture composition, giving the fraction of the material that comes from the fuel stream; and its so-called scalar dissipation, $\chi = 2D\nabla Z \cdot \nabla Z$ (in which D is its molecular diffusivity), χ being related to the rate of dissipation of fluctuations of Z in turbulent flow. Since many chemical length scales are often several orders of magnitude smaller than the turbulent length scales in real applications, modelling of Z with a thin reaction sheet at its stoichiometric surface can be a reasonable approach that helps to separate the chemistry from the turbulence. Knowledge of Z and χ in turbulent flows is important for testing the validity of various models, such as the laminar flamelet model (Williams 1975; Peters 1984, 1986), the conditional moment closure (CMC) model (Klimenko 1990; Bilger 1993) and models based on integration of the transport equation for the probability-density function (p.d.f. approaches) (Kollmann & Janicka 1982; Pope 1985). The present paper reports DNS

† Current address: Graduate Aeronautical Laboratories, California Institute of Technology, 205-45, Pasadena, CA, 91125, USA.
‡ Author to whom correspondence should be addressed: ssarkar@ucsd.edu

results for Z and χ in the reaction-sheet approximation (Burke & Schumann 1928) and explores statistical aspects that are relevant to these models.

The statistics of Z and χ can be expressed in terms of the joint probability-density function (p.d.f.) of these two scalars, $P(Z, \chi)$. Such p.d.f.s depend, in general, on the spatial position, x, and time, t, but for brevity of notation these dependences will not be exhibited explicitly. The expected value of a function of Z and χ, $\psi(Z, \chi)$, is readily calculated from $P(Z, \chi)$ as

$$\bar{\psi} = \langle \psi \rangle = \int_0^1 \int_0^\infty \psi(Z, \chi) P(Z, \chi) \, d\chi \, dZ. \tag{1.1}$$

Different expectation values are of interest in different approaches to modelling of turbulent combustion.

In the simplest laminar flamelet model, species mass fractions, Y_i, for species i, temperature, T, and density, ρ, explicitly depend only on Z, causing the marginal p.d.f. $P(Z) = \int_0^\infty P(Z, \chi) \, d\chi$ to be relevant for obtaining their expectation values, as well as for obtaining the expectation value of the rate, $\omega_k(Y_i, T, \rho)$, of any reaction, k. In the fast-chemistry (reaction-sheet) approximation of flamelet models, however, the overall rate of heat release at the reaction sheet is proportional to the conditionally averaged scalar dissipation there,

$$\langle \chi | Z \rangle = \int_0^\infty \chi P(\chi | Z) \, d\chi = \int_0^\infty \chi \frac{P(Z, \chi)}{P(Z)} \, d\chi \tag{1.2}$$

(Bilger 1976a, b). The CMC model in non-premixed turbulent combustion similarly requires $\langle \chi | Z \rangle$ for integrating transport equations for the conditional averages $\langle Y_i | Z \rangle$ (Bilger 1993), prior to obtaining the expectation value by evaluating $\bar{Y}_i = \int_0^1 \langle Y_i | Z \rangle P(Z) \, dZ$. Since p.d.f. approaches also model $\langle \chi | Z \rangle$ (as well as χ conditioned on other scalars, Pope 1985), joint statistics of Z and χ are obviously of interest for all of these approaches.

In their review of direct numerical simulations (DNS) of non-premixed turbulent combustion Vervisch & Poinsot (1998) identify four different types of relevant analysis. Since the fourth type concerns effects of finite-rate chemistry, the present study has no direct bearing on this. It does, however, pertain to the first three types, namely Z contours, behaviour in directions normal to constant-Z surfaces and one-point statistics. Especially in the second of these categories, new information concerning variations of both Z and χ fields in normal directions is obtained, mostly at turbulence Reynolds numbers higher than any previously available.

The strong heat release typical of turbulent combustion affects the turbulent flow field mainly by reducing the density, increasing the kinematic viscosity and, secondarily, by altering the local pressure gradient. Exactly how these influences occur, however, is not well understood. DNS, experiment and modelling all can help provide clarification. In the present paper discussion is devoted mainly to DNS because it is the main focus of this work. While there have been many relevant DNS studies, most pertain to relatively small or zero heat release and therefore cannot fully address the influences on the turbulence. They can, however, provide important information on statistics of mixture fraction and scalar dissipation, and therefore they are considered here as well.

Scalar fields that do not affect pressure, density or velocity fields in any way will be termed passive, while those that do will be called active. Scalar fields having non-zero chemical source terms of finite or infinite rate will be termed reactive, even though at infinite rates the problem can be reformulated with non-reactive

scalars having more complicated thermodynamics. DNS has addressed passive, non-reactive scalars (Kerr 1985; Ashurst *et al.* 1987; Eswaran & Pope 1988; Nomura & Elghobashi 1992; Rogers & Moser 1994; Overholt & Pope 1996; Juneja & Pope 1996; Stanley, Sarkar & Mellado 2002), passive reactive scalars (Riley, Metcalfe & Orszag 1986; Leonard & Hill 1991; Montgomery, Kosály & Riley 1993; Mell *et al.* 1994; Lee & Pope 1995; Swaminathan & Bilger 1997; Overholt & Pope 1999), active, non-reactive scalars (de Bruyn Kops & Riley 2000; Pantano & Sarkar 2002) and active reactive scalars (McMurtry, Riley & Metcalfe 1989; Miller, Madnia & Givi 1994; Balakrishnan, Sarkar & Williams 1995; Mahalingam, Chen & Vervisch 1995; Swaminathan, Mahalingam & Kerr 1996; Montgomery, Kosály & Riley 1997; Livescu, Jaberi & Madnia 2002); much of this research has been discussed in reviews (Jou & Riley 1989; Givi 1989; Vervisch & Poinsot 1998). The flow configurations considered range from homogeneous, isotropic turbulence (Kerr 1985; Ashurst *et al.* 1987; Eswaran & Pope 1988; Leonard & Hill 1991; Nomura & Elghobashi 1992; Montgomery *et al.* 1993; Mell *et al.* 1994; Lee & Pope 1995; Mahalingam *et al.* 1995; Overholt & Pope 1996; Juneja & Pope 1996; Swaminathan *et al.* 1996; Montgomery *et al.* 1997; Swaminathan & Bilger 1997; Overholt & Pope 1999; de Bruyn Kops & Riley 2000; Livescu *et al.* 2002) to temporally evolving turbulent shear layers (Riley *et al.* 1986; McMurtry *et al.* 1989; Rogers & Moser 1994; Miller *et al.* 1994) and turbulent planar jets (Stanley *et al.* 2002). A great deal of information can be gleaned from these works.

Many earlier investigations, not cited, employed two-dimensional turbulence simulations. This approximation excludes vortex stretching and is now known to overestimate effects of baroclinicity in variable-density turbulent diffusion flames. Attention therefore is restricted to fully three-dimensional simulations. The current study concerns mainly active, reactive, temporally evolving shear layers. Previous three-dimensional simulations of this kind were done by Riley *et al.* (1986), McMurtry *et al.* (1989) and Miller *et al.* (1994).

Building on the work of Riley *et al.* (1986), McMurtry *et al.* (1989) considered moderate heat release in an ideal gas, $T_{max}/T_o = 2$, where T_{max} is the peak temperature and T_o is the reference low temperature. They used a spatial grid of 64^3 points, typical of that time, and they focused on the turbulence energetics and vortex dynamics, treating a one-step, irreversible reaction having a Damköhler number (the ratio of the large-eddy turnover time to the chemical e-folding time) of $Da = 2$. Miller *et al.* (1994) also considered a one-step irreversible reaction, but with various values of Da, although for low heat release, $T_{max}/T_o = 1.2$, using as many as $150 \times 150 \times 90$ grid points. These two previous studies of reacting shear layers have mainly concentrated on effects of heat release, a common conclusion being that entrainment rates and the growth of the shear-layer thickness decrease with increasing heat release. The present work addresses only the limit $Da \to \infty$ but considers more realistic heat release, up to $T_{max}/T_o \simeq 7$, employing as many as $768 \times 258 \times 192$ grid points. It thereby extends the database to heat-release values of practical interest, with good resolution.

A fully compressible code is employed in the present work, with a convective Mach number (Bogdanoff 1983; Papamoschou & Roshko 1988) defined as $M_c = \Delta u/(c_1 + c_2)$ (where Δu is the velocity difference of the two streams, and c_1 and c_2 are the speeds of sound of each stream) equal to 0.3 in all cases. This value is small enough that compressibility effects from Mach number are not important. More precisely, the compressibility effects contribute less than 10% to T and ρ or any flow properties investigated, their relative influence being of order $\frac{1}{2}(\gamma - 1)M^2$, where γ is a representative ratio of specific heats and M a representative Mach number, $M \approx 2M_c$

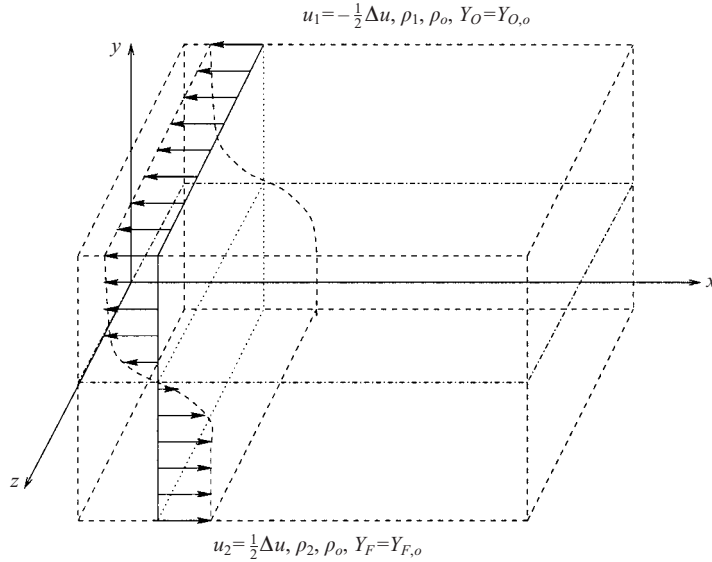$$u_1 = -\tfrac{1}{2}\Delta u, \rho_1, \rho_o, Y_O = Y_{O,o}$$

FIGURE 1. Schematic diagram of the temporally evolving shear layer
($x = x_1$, $y = x_2$ and $z = x_3$).

(the simulations have $\gamma \approx 1.4$ and $M \approx 0.7$). Exploratory calculations at other Mach numbers verified compressibility to be unimportant for all results reported here.

To help clarify influence of heat release, DNS results are reported here for three different levels of heat release. A number of questions are addressed. How does heat release change the scaling of the micromixing time scale, as measured by the scalar dissipation normalized by outer flow variables? How do scalar statistics change with heat release? What is the effect of heat release on the conditional scalar dissipation? How is the average reaction-rate term affected by heat release? What are the statistics of the scalar field at the flame? How is the mechanical-to-scalar time-scale ratio affected by heat release? What are the differences between laminar and turbulent mixing at the stoichiometric surface?

2. The flow addressed

Figure 1 is a sketch of the flow configuration considered. The upper stream is air (approximated as a mixture of oxygen and nitrogen with an oxygen mass fraction of 0.23) and the lower a mixture of methane and nitrogen with a methane mass fraction of 0.23. The latter value was chosen because the chemistry that occurs at the reaction sheet, $CH_4 + 2O_2 \rightarrow CO_2 + 2H_2O$, then yields a stoichiometric mixture fraction $Z_s = 0.2$, that is the Burke–Schumann sheet which exists at $Z = Z_s$ and into which CH_4 and O_2 diffuse in stoichiometric proportions from opposite directions, is at $Z = 0.2$, as is seen in figure 2. For the more usual case of pure methane reacting with the air stream, $Z_s = 0.054$, which is too small for convenient resolution of the temperature gradient on the air side in the simulation. Since a symmetric problem, $Z_s = 0.5$, is atypical of most real fuel–air or fuel–oxygen combustion situations, the value $Z_s = 0.2$ is selected as a compromise that preserves the qualitative effects of real stoichiometry while affording good DNS resolution. There is, in addition, some
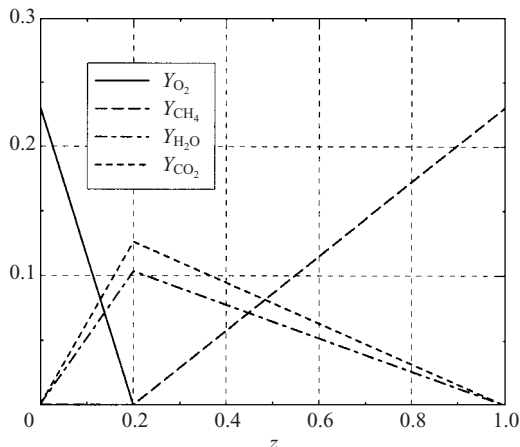
FIGURE 2. Dependence of the mass fractions on the mixture fraction.

interest in the combustion of inert-diluted fuels, for example to achieve pollutant reduction, for which the simulation would be more accurate.

To eliminate effects of density differences of the two streams, they are required to have equal densities, ρ_o, in all simulations. This forces the influence of density variations to be associated exclusively with the heat release in combustion, the effects of which the study is designed to address. Since the fluid is taken to be an ideal-gas mixture, and pressure is nearly constant because of sufficiently low Mach numbers, the fact that the fuel has a lower molecular weight than oxygen then requires the temperature of the air stream to exceed that of the fuel stream. The oxidizer side thus has a temperature approximately 20% higher than the fuel side for the reactants considered, but the difference is sufficiently small that its effects on the results are negligible; in fact, for these mixtures, the results would have been essentially the same if the two streams had the same temperature but different densities. The temperature of the fuel stream is $T_o = 298\,\mathrm{K}$ in the simulations, but, again, the results are expected to be quite representative of any such gaseous systems with boundary temperature below about 600 K, above which some fuel-pyrolysis chemistry and enhanced dissociation at the flame may begin. Although attention is focused on streams at normal atmospheric pressure, the results should apply whenever the gas mixture is ideal, certainly at any pressure below 10 bar.

Specific heats of the species in the ideal-gas mixture are allowed to depend on temperature, to maintain correct cold-gas values and avoid achieving flame temperatures that are too high at the reaction sheet, which would result in gas densities too low there. From thermochemical data (Lide 1999), linear dependences of specific heats on temperature were constructed over the temperature range of interest (about 300 to 2300 K). Table 1 summarizes the resulting coefficients in non-dimensional form. In that table, C_p^0 denotes the value at 298 K and C_p^1 the coefficient of the term linear in the temperature non-dimensionalized by T_o, that is the non-dimensional specific heat of species i is $C_{pi} = C_{pi}^0 + C_{pi}^1(T/T_o - 1)$. Also listed in the table are non-dimensionalized standard enthalpies of formation Δh^o and molecular weights W ($\mathrm{g\,mol^{-1}}$), obtained from the same source and used in the simulations. The values of the parameters in table 1 give an adiabatic flame temperature for $Z_s = 0.2$ of $T_f = 2028\,\mathrm{K}$.

Species	C_p^0	C_p^1	W	$\Delta h^0/C_{pO_o}T_o$
CH_4	2.4655	0.8743	16	-17.149
O_2	1.0000	0.0639	32	0
H_2O	2.0110	0.2187	18	-49.814
CO_2	0.9347	0.1321	44	-33.168
N_2	1.1397	0.0553	28	0

TABLE 1. Thermochemical parameters; the reference temperature is $T_o = 298\,\text{K}$, and the reference specific heat is that of oxygen at this temperature, $C_{pO_o} = 905\,\text{J}\,\text{kg}^{-1}\,\text{K}^{-1}$.

To clarify interpretations by focusing attention on as few different physical phenomena as possible, simplifications were introduced in molecular transport properties. All chemical species were assumed to have the same diffusion coefficient, D, so that all mass fractions are completely determined by Z, as shown in figure 2 (Williams 1985), and effects of differential diffusion are thereby eliminated; generalized Burke–Schumann formulations (Sanchez, Liñán & Williams 1997) were not considered because they necessitate using more than one variable of the mixture-fraction type, and such effects are expected to be small for methane–air mixtures. The viscosity μ was taken to be constant, to eliminate the effect on the Reynolds number of the increase of viscosity with increasing temperature. Since viscosity is proportional to temperature to a power between zero and unity, the resulting tendency towards 'laminarization' at high temperatures through reduced Reynolds numbers is not likely to be extremely large and is purposely eliminated by this approximation. There is, nevertheless, a reduction of the Reynolds number caused by the variations of density through the increase in the kinematic viscosity, $\nu = \mu/\rho$. The product ρD is also assumed constant, so that the Schmidt number, $Sc = \mu/\rho D$, is constant. Also imposed is constancy of the Prandtl number, $Pr = \mu C_p/\kappa$, where κ denotes the thermal conductivity. Because of the variations of the specific heat C_p of the mixture, κ also varies to maintain Pr constant at constant μ. The approximate value for air, $Pr = 0.7$, is employed throughout, while the value $Sc = 1.0$ is used in the simulations without chemical heat release. On the other hand, $Sc = 0.7$ for the simulations with heat release, a selection made to achieve a Lewis number (Sc/Pr) of unity, thereby allowing the temperature also to be related uniquely to Z at low Mach numbers with radiant energy loss neglected (Williams 1985). The simulation without heat release is based on earlier work (Pantano & Sarkar 2002) for which Lewis numbers were irrelevant and $Sc = 1.0$ was employed; the two different values of Sc in the present study are close enough that none of the effects investigated depend measurably on this difference.

In the temporally evolving shear layer, the average values depend on x_2 (the inhomogeneous direction of the flow) and time. Averages therefore are calculated as planar averages in the uniform directions, x_1 and x_3. Both the customary Reynolds average, $\bar{\psi}$, and the density-weighted or Favre average, $\tilde{\psi}$, defined as

$$\tilde{\psi} = \frac{\overline{\rho\psi}}{\bar{\rho}} \qquad (2.1)$$

are used in the paper. Fluctuations with respect to the mean are represented by $\psi' = \psi - \bar{\psi}$ for the Reynolds averages and by $\psi'' = \psi - \tilde{\psi}$ for the Favre averages.

3. Mathematical formulation, approach and parameters

The unsteady, three-dimensional, compressible Navier–Stokes equations for a Newtonian fluid composed of a reacting ideal-gas mixture are considered in this study. Energy conservation is written as a pressure equation to facilitate computation. Relevant parameters are the Reynolds number,

$$Re = \frac{\rho_o \Delta u \delta_{\omega,o}}{\mu}, \tag{3.1}$$

and the non-dimensional heat release,

$$Q = \frac{q_o Y_{F,f} Z_s}{C_{pN_o} T_o \nu_F W_F}. \tag{3.2}$$

In (3.1) the characteristic length $\delta_{\omega,o}$ is the initial vorticity thickness of the shear layer, defined as

$$\delta_\omega = \frac{\Delta u}{(\partial \tilde{u}_1/\partial x_2)_{max}}, \tag{3.3}$$

where $\tilde{u}_1$ is the Favre-averaged velocity in the x_1-direction, and in (3.2) q_o denotes the enthalpy of the reaction (Williams 1985),

$$q_o = \sum \nu_i W_i \Delta h_i^o. \tag{3.4}$$

W_i is the molecular weight of species i, $\nu_{CH_4} = \nu_F = 1$, $\nu_{O_2} = \nu_O = 2$, $\nu_{CO_2} = -1$, $\nu_{H_2O} = -2$ and C_{pN_o} is the specific heat of nitrogen at T_o. The formulation is non-dimensional, the unit length being $\delta_{\omega,o}$, velocity Δu, time $\delta_{\omega,o}/\Delta u$, density ρ_o, temperature T_o, enthalpy $C_{pO_o} T_o$ and pressure $\rho_o \Delta u^2$.

The relationships

$$Y_O(Z) = Y_O^e(Z) \equiv \begin{cases} Y_{O,o}(1+\phi)(Z_s - Z) & \text{if } Z < Z_s \\ 0 & \text{if } Z > Z_s, \end{cases} \tag{3.5}$$

$$Y_F(Z) = Y_F^e(Z) \equiv \begin{cases} 0 & \text{if } Z < Z_s \\ Y_{F,f}\dfrac{(1+\phi)}{\phi}(Z - Z_s) & \text{if } Z > Z_s, \end{cases} \tag{3.6}$$

where $\phi = (W_O \nu_O Y_{F,f})/(W_F \nu_F Y_{O,o}) = (1 - Z_s)/Z_s$ is the fuel–air equivalence ratio, and

$$Y_p(Z) = Y_p^e(Z) = \frac{W_p \nu_p Y_{F,f}}{W_F}\left(Z - \frac{Y_F^e(Z)}{Y_{F,f}}\right), \quad p = CO_2, H_2O \tag{3.7}$$

apply (Williams 1985), and

$$Y_{N_2} = 1 - \sum_{i \neq N_2} Y_i. \tag{3.8}$$

Here, the subscripts O and F stand for oxidizer, O_2, and fuel, CH_4, respectively, and $Y_{O,o}$ is the mass fraction of the oxidizer in the oxidizer stream, while $Y_{F,f}$ is the mass fraction of fuel in the fuel stream.

As previously indicated, in the limit of low Mach numbers, with radiant energy loss neglected, enthalpy and temperature also are related uniquely to Z. The corresponding non-dimensional relations will be denoted by $h^e(Z)$ and $T^e(Z)$, where (Williams 1985)

$$h^e(Z) = h_O + (h_F - h_O)Z, \tag{3.9}$$

the subscript O and F identifying conditions in oxidizer and fuel streams respectively. This result for $h^e(Z)$ determines $T^e(Z)$ through (3.5)–(3.8) and the thermochemistry.

Since the non-dimensional pressure, p, also becomes constant in this limit, from the ideal-gas equation of state, the non-dimensional density becomes

$$\rho^e(Z) = \frac{p\gamma_o M^2 \overline{W}(Z)}{T^e(Z)}, \tag{3.10}$$

where the Mach number is $M = \Delta u / \sqrt{\gamma_o R_o T_o}$, γ_o and R_o being the ratio of specific heats and gas constant for O_2 at T_o, and the normalized average molecular weight is

$$\overline{W} = \left(W_O \sum_1^N \frac{Y_i}{W_i} \right)^{-1}. \tag{3.11}$$

In the present simulations h and ρ are not given by (3.9)–(3.10), that is, h and ρ are not explicit functions of Z. Instead, the corresponding mass and energy transport equations are solved.

The conservation equation for Z is

$$\frac{\partial(\rho Z)}{\partial t} + \frac{\partial(\rho Z u_k)}{\partial x_k} = \frac{1}{ReSc} \frac{\partial}{\partial x_k} \left(\frac{\partial Z}{\partial x_k} \right), \tag{3.12}$$

all species mass fractions being determined uniquely by Z from the preceding formulas. The conservation equations for mass, momentum and energy are

$$\frac{\partial \rho}{\partial t} + \frac{\partial(\rho u_k)}{\partial x_k} = 0, \tag{3.13}$$

$$\frac{\partial(\rho u_i)}{\partial t} + \frac{\partial(\rho u_k u_i)}{\partial x_k} = -\frac{\partial p}{\partial x_i} + \frac{\partial \sigma_{ik}}{\partial x_k}, \tag{3.14}$$

and

$$\frac{\partial p}{\partial t} + u_k \frac{\partial p}{\partial x_k} = -\gamma p \frac{\partial u_k}{\partial x_k} + \frac{(\gamma - 1)}{(\gamma_o - 1)RePrM^2} \frac{\partial}{\partial x_k} \left(\frac{\partial h}{\partial x_k} \right) + (\gamma - 1)\Phi$$

$$+ \frac{\gamma}{\gamma_o ReScM^2} \left(T \sum_1^N \frac{W_O}{W_i} \frac{dY_i^e}{dZ} - \frac{1}{\overline{W}\overline{C}_p} \sum_1^N h_i \frac{dY_i^e}{dZ} \right) \frac{\partial}{\partial x_k} \left(\frac{\partial Z}{\partial x_k} \right). \tag{3.15}$$

In (3.14) the viscous stress tensor is given by

$$\sigma_{ij} = \frac{1}{Re} \left\{ \frac{\partial u_i}{\partial x_j} + \frac{\partial u_j}{\partial x_i} - \frac{2}{3} \frac{\partial u_k}{\partial x_k} \delta_{ij} \right\}, \tag{3.16}$$

and in (3.15) the viscous dissipation is

$$\Phi = \sigma_{ij} \frac{\partial u_i}{\partial x_j}. \tag{3.17}$$

Appearing in (3.15) is the non-dimensional mixture enthalpy

$$h = \sum_1^N h_i Y_i, \tag{3.18}$$

in which

$$h_i = \frac{\Delta h_i^o}{C_{pO_o} T_o} + \int_1^T C_{pi}(T) \, dT. \tag{3.19}$$

The non-dimensional average specific heat of the mixture is

$$\bar{C}_p = \sum_1^N C_{pi}(T) Y_i. \tag{3.20}$$

The non-dimensional equation of state of the mixture is

$$p = \frac{\rho T}{\gamma_o M^2 \overline{\overline{W}}}. \tag{3.21}$$

The specific heat ratio of the mixture, γ, varies somewhat and is given by

$$\gamma = \frac{\gamma_o}{\gamma_o - (\gamma_o - 1)/(\overline{W}\bar{C}_p)}. \tag{3.22}$$

The heat-release parameter Q of (3.2) would be equal to $T_f/T_o - 1$ if the specific heat of the mixture were constant. Numerically Q is somewhat larger because of the variable specific heat. Simulations were performed for the values $Q = 0$, $Q = 3.73$ and $Q = 7.46$. To achieve these values in the computation, the values of Δh_i^o in (3.4) were all adjusted proportionally from the values listed in table 1; the values in that table give a value of Q from (3.2) equal to 7.46, so that the largest Q is more realistic. For $Q \neq 0$, the differential equations (3.12)–(3.15) are coupled because h and Z appear on the right-hand side of (3.15), with h given by (3.18), in which Y_i is determined by Z while h_i is determined by T, dependent on p, ρ and Z through (3.21). For $Q = 0$, temperature variations are much smaller, and therefore the approximation of constant specific heats was employed, leading to $\gamma = \gamma_o$ and

$$h = \gamma_0 M^2 \frac{p}{\rho}, \tag{3.23}$$

which does not involve Z and which therefore enables (3.13)–(3.17) to be solved without considering (3.12), thereby decoupling variations of mixture fraction and species concentrations from the fluid-mechanics problem.

3.1. *Numerical scheme and flow initialization*

The calculation proceeds in the following way: suppose that the variables ρ, p, u_i and Z are available at a given time. The temperature is obtained from (3.21) after using (3.5)–(3.7) and (3.11). The enthalpy is then computed from (3.18)–(3.19). Finally, (3.12)–(3.15) are solved using explicit time integration to advance the variables in time.

The transport equations are integrated using a compact Padé scheme in space with sixth-order of accuracy (Lele 1992). The time advancement is performed with a fourth-order low-storage Runge–Kutta scheme (Williamson 1980). The coordinates x_1, x_2 and x_3 are referred to also as x, y and z, respectively, throughout the text. Periodic boundary conditions in the x_1- and x_3-directions are used and 'non-reflective' boundary conditions are imposed in the x_2-direction (Thompson 1987). The grid is uniform in the x_1- and x_3-directions with an equal grid spacing, Δx, in both directions. In the transverse direction, x_2, the grid is uniform across the centre of the domain enclosing the thickness of the shear layer, even at the last time of the calculation, and it is stretched gradually in the rest of the domain. The grid spacing in the centre of the domain in the transverse direction is also Δx, while the stretching in the external part of the domain is 1%. In the simulations with heat release, the mass fractions of all species are smoothed around Z_s (Higuera & Moser 1994) to allow numerical resolution of the discontinuities in the mass-fraction gradients at Z_s. This small difficulty arises from the Burke–Schumann approximation (Sepri 1976) and can be

handled numerically. It can be verified that the mass fraction of species i approaches the values given by the Burke–Schumann solution away from the flame sheet when the mass-fraction gradient is defined as

$$\frac{\mathrm{d}Y_i}{\mathrm{d}Z} = \frac{1}{\delta}\left\{\frac{\mathrm{d}Y_i}{\mathrm{d}Z}\bigg|_o + \frac{1}{2}\left(\frac{\mathrm{d}Y_i}{\mathrm{d}Z}\bigg|_f - \frac{\mathrm{d}Y_i}{\mathrm{d}Z}\bigg|_o\right)\left(1 + \tanh\left(\frac{Z - Z_s}{\delta}\right)\right)\right\}, \qquad (3.24)$$

where δ is a smoothing factor and $\mathrm{d}Y_i/\mathrm{d}Z|_o$ and $\mathrm{d}Y_i/\mathrm{d}Z|_f$ are the mass-fraction gradients on the oxidizer and the fuel sides, respectively, given by (3.5)–(3.7). Exploratory calculations showed that a value of δ equal to 0.02 did not affect the dynamics of the flow, as shown by Higuera & Moser (1994), and this value was used in all the simulations.

The flow is initialized to a hyperbolic-tangent profile for the mean streamwise velocity, $\bar{u}_1(x_2)$, while all other mean velocity components are set to zero. Thus,

$$\bar{u}_1(x_2) = \tfrac{1}{2}\tanh\left(-\frac{x_2}{2\delta_o}\right), \quad \bar{u}_2 = 0, \quad \bar{u}_3 = 0, \qquad (3.25)$$

the value $\delta_o = 0.227\delta_{\omega,0}$ being employed in the simulations. The mean pressure is set initially to a uniform value and $\rho_1 = \rho_2 = 1$ throughout. In addition to the mean fields, broadband fluctuations are used to accelerate the transition to turbulence. This is achieved by generating a random velocity field with an isotropic turbulence spectrum of the form

$$E(k) = (k/k_o)^4 \exp\left(-2(k/k_o)^2\right), \qquad (3.26)$$

where k is the wavenumber and k_o the wavenumber of peak energy. The extent of the initial velocity fluctuations is limited in the cross-stream direction by an exponential decay given by

$$\exp\left(-(x_2/\delta_b)^2\right) \qquad (3.27)$$

where δ_b is δ_o in the simulation without heat release and $4\delta_o$ in the simulations with heat release. A larger value of δ_b is needed with heat release to excite the most unstable modes of the shear layer that are then located away from the centre of the shear layer (Planché 1992). Without heat release, with equal-density streams, the most unstable mode is located at the centre of the shear layer. Solenoidality is imposed on this random turbulent field. Such quasi-incompressible fluctuations minimize compressibility transients (Erlebacher *et al.* 1990). The initial pressure fluctuations are obtained from the Poisson equation for incompressible flow.

The mean scalar field is initialized to

$$\bar{Z}(x_2) = \frac{1}{2}\left(1 + \tanh\left(-\frac{x_2}{2\delta_o}\right)\right), \qquad (3.28)$$

and the initial scalar fluctuations are set to zero. Prescription of the initial scalar field gives initial distributions of Y_i and $\overline{W}$ from previous equations, and the approximation $T = T^e(Z)$ is then used in (3.21) to initialize ρ. For zero heat release, the isentropic relation, p/ρ^γ constant, is employed instead to initialize ρ.

3.2. *Parameters of the simulations*

Table 2 summarizes the parameters of the three simulations. The domain size is similar in all calculations but the number of grid points was larger in the simulations with heat release. This ensured better resolution of the sharp density and temperature gradients at the flame sheet, a restriction not encountered in case A. Since the kinematic viscosity increases with temperature, the Reynolds number, *Re*, was deliberately kept

Case	A	B	C
Q	0.0	3.73	7.46
Re	672	5280	5280
$k_o \delta_{\omega,o}$	3.73	9.61	9.70
$L_x/\delta_{\omega,0}$	81	31	31
$L_y/\delta_{\omega,0}$	40	20	20
$L_z/\delta_{\omega,0}$	20	8	8
$N_x\ N_y\ N_z$	$512 \times 256 \times 128$	$768 \times 258 \times 192$	$768 \times 258 \times 192$

TABLE 2. Initial parameters of the simulations. The computational domain has dimensions L_x, L_y and L_z with N_x, N_y and N_z grid points, respectively.

Case	A	B	C
Re_ω	5700	12 600	10 400
$\tilde{k}_{peak}/\Delta u^2$	0.033	0.022	0.023
$\tilde{\epsilon}_{peak}\delta_\omega/\Delta u^3$	6.55×10^{-3}	4.89×10^{-3}	4.40×10^{-3}
$Re_{\lambda,peak}$	138	104	82
$Re_{\lambda,f}$	103	96	63
$\tilde{\chi}_{peak}\delta_\omega/\Delta u$	13.8×10^{-3}	11.1×10^{-3}	9.7×10^{-3}
$\eta_{min}/\Delta x$	0.29	0.36	0.46
$\eta_f/\Delta x$	0.36	0.46	0.60
r_{avg}	1.31	1.69	1.60
r_{peak}	1.55	1.93	1.84

TABLE 3. Final parameters of the simulations. The subscript 'peak' identifies the largest value encountered in the shear layer, $Re_{\lambda,f}$ denotes the microscale Reynolds number at the mean flame position, η_{min} is the minimum value of the Kolmogorov scale across the shear layer, and η_f is the Kolmogorov scale at the mean flame position. Here r_{avg} denotes the average (over the shear layer) of the mechanical-to-scalar time-scale ratio.

larger in the reactive cases and was selected to achieve similar microscale Reynolds numbers, Re_λ, at the stoichiometric location in all three cases. Details of case A are fully described by Pantano & Sarkar (2002) as case A3 in that paper. The Mach number that appears in (3.15) was set to $M = 0.694$.

Since the flow evolves with time, exhibiting a shear-layer thickness that increases with time, the largest Reynolds number is achieved at the end of the calculations. This final Reynolds number is denoted by

$$Re_\omega = Re\frac{\delta_\omega}{\delta_{\omega,0}}. \tag{3.29}$$

Table 3 gives values of turbulence parameters at this Reynolds number, including the turbulent kinetic energy, defined in terms of Favre fluctuations,

$$\tilde{k} = \frac{\widetilde{u_i'' u_i''}}{2}, \tag{3.30}$$

and the turbulent dissipation rate, $\tilde{\epsilon}$, defined as

$$\tilde{\epsilon} = \frac{1}{\bar{\rho}}\overline{\left(\sigma_{ik}'\frac{\partial u_i'}{\partial x_k}\right)}. \tag{3.31}$$

Values of $\tilde{\epsilon}$ are used to calculate the Taylor microscale, λ, from the isotropic relationship

$$\tilde{\epsilon} = 15\nu\frac{u^2}{\lambda^2} = 5\nu\frac{q^2}{\lambda^2},$$

where the turbulence intensity is defined as $q = \sqrt{2\tilde{k}/3}$, which was equal to $0.1\Delta u$ initially. The Taylor microscale and the turbulence intensity can be combined to construct a microscale Reynolds number given by

$$Re_\lambda = \frac{q\lambda}{\nu} = 2\tilde{k}\sqrt{\frac{5}{\nu\tilde{\epsilon}}}. \tag{3.32}$$

Similarly, the averaged scalar dissipation is defined by

$$\tilde{\chi} = \frac{2}{\bar{\rho}ReSc}\overline{\frac{\partial Z'}{\partial x_k}\frac{\partial Z'}{\partial x_k}}. \tag{3.33}$$

Characteristic values of the Kolmogorov scale, η, defined as $\eta = (\nu^3/\tilde{\epsilon})^{1/4}$, are also given in table 3. Higher resolution of small-scale turbulence is required in the reactive cases, and therefore the value $\eta/\Delta x = 0.6$ at the flame in case C is larger than the value $\eta/\Delta x = 0.29$ in case A. These values are sufficient for DNS simulations (Moin & Mahesh 1998). The table also gives values of the quantity r, important for modelling a conserved scalar in turbulent flow, that denotes the ratio of the mechanical time scale, $\tilde{k}/\tilde{\epsilon}$, to the scalar time scale, $\widetilde{Z''^2}/\tilde{\chi}$.

4. Average state relations

The change of density by heat release is a key aspect of how combustion modifies turbulent flow. In presenting results, we therefore consider first the instantaneous density field and the average density conditioned on mixture fraction. Explicit dependences of scalars on mixture fraction, as in (3.5)–(3.7), (3.9) and (3.10), are often called state relations, and there is interest in knowing how well various state relations may apply in turbulent flows. State relations, especially for the density, are discussed here.

To see how heat release affects turbulence, it is helpful to consider instantaneous temperature and density fields for the largest heat release, simulation C. Figure 3 shows such a result, for a vertical cut through the shear layer, taken at the end of the simulation. The vertical extent of the computational domain was approximately three times the distance seen in the figure, whence the box size had negligible influence on the development of the turbulence. There are striking differences between the temperature and the density fields in figure 3. The regions of maximum temperature coincide closely with the regions of minimum density, as would be expected for reaction sheets in isobaric flow, but on the fuel side of these reaction sheets (bottom stream), the density remains low over an appreciably wider region than that over which the temperature remains high. The result is a fairly extended region of low density in the centre of the shear layer, in contrast to the temperature, which peaks more sharply at the reaction sheet. It will be seen later that the extended low-density region profoundly affects the turbulent mixing.

The reason for the difference between the temperature and density fields becomes clear upon examining the state relations. In the problem addressed, the species mass fraction, and therefore the mean molecular weight, obey perfect state relations. As seen in figure 4, the associated variation of $\overline{W}$ is small. In isobaric flows of low
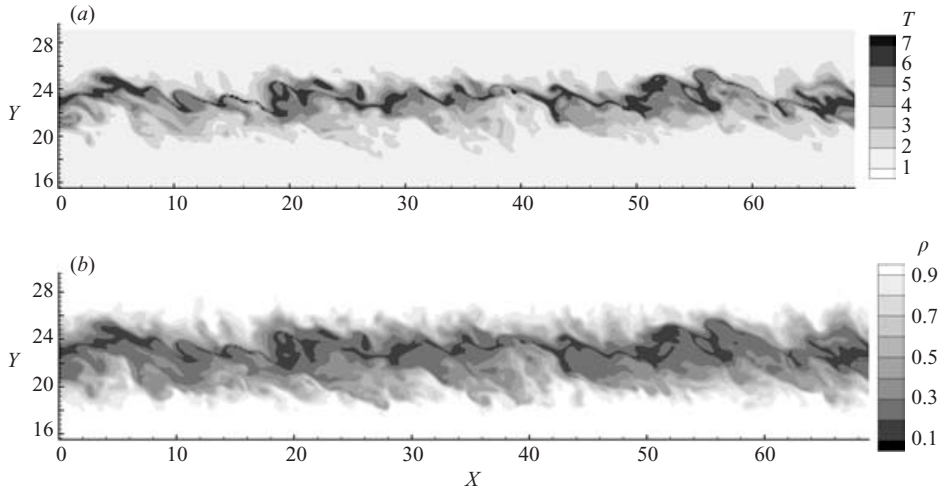
FIGURE 3. Isocontours for simulation C (maximum heat release): vertical cuts of (*a*) instantaneous temperature and (*b*) instantaneous density.
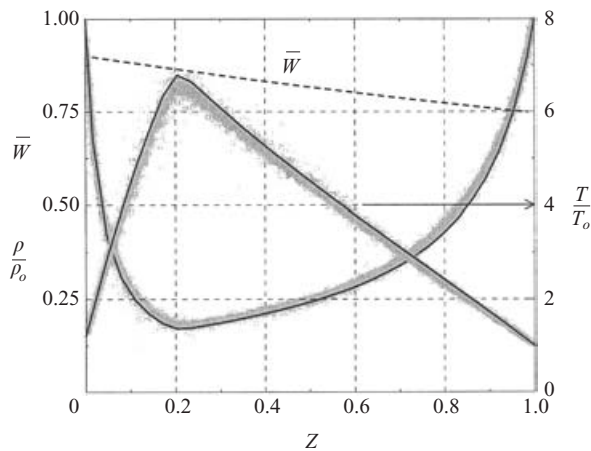

FIGURE 4. Scatter plot of the density and temperature and their corresponding Burke–Schumann limits (thick curves) for simulation C, as well as the non-dimensional average molecular weight for all simulations.

Mach number, M, it was seen in (3.9) that $T(Z) = T^e(Z)$ also obeys a perfect state relationship, with a nearly piecewise linear dependence, resulting from the linearity of $h^e(Z)$; the small departures from piecewise linearity for $T(Z)$ are due to the dependence of the specific heats on temperature. The scatter plot of $T(Z)$ from the DNS, shown in figure 4, demonstrates that, in the turbulent flow considered here, this state relation continues to apply, to a good approximation, on a space–time-resolved basis, with departures only on the order of 10%. The points cluster closely around the curve $T^e(Z)$, with departures approximately equally above and below the curve. This is to be expected because the differences, which are associated only with compressibility and viscous dissipation, should be of order $\frac{1}{2}(\gamma - 1)M^2$, approximately 0.1 for $M = 0.7$ and $\gamma = 1.4$.
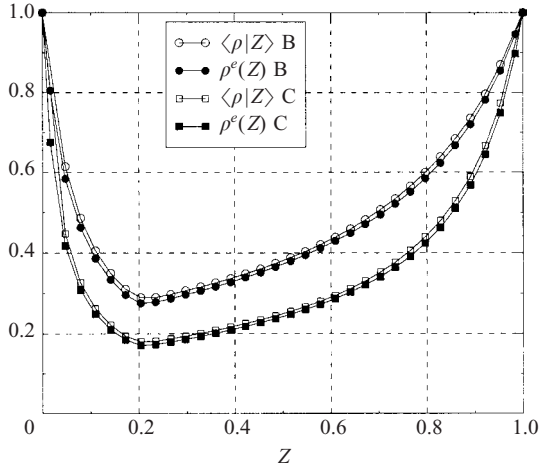
FIGURE 5. Conditional average density and equilibrium density as functions of mixture
fraction for different levels of heat release for simulations B and C.

Given the state-relation agreements of $Y_i(Z)$ and $T(Z)$, the corresponding agreement of $\rho(Z)$, also seen in figure 4, is to be expected from the equation of state (3.21), since the compressible pressure fluctuations are also of order $\frac{1}{2}(\gamma - 1)M^2$. It thus becomes clear that the shape of the curve of $\rho^e(Z)$ is responsible for the differences between T and ρ seen in figures 3 and 4. Specifically, the proportionality $\rho \sim 1/T$, that applies because variations of p and $\overline{W}$ are small, leads to the flat portions of the $\rho^e(Z)$ curve on the fuel side of the stoichiometric surface in figure 4. This observation enables us to deduce how the results would change if the stoichiometric mixture fraction were different from the value $Z_s = 0.2$ of the simulations. For smaller Z_s, the density would decrease more sharply with increasing Z near $Z = 0$, leading to a wider low-density region. Even for the symmetric case $Z_s = 0.5$, the low-density region would be larger than the high-temperature region as a consequence of the $\rho \sim 1/T$ approximate proportionality. To further emphasize the closeness of ρ to $\rho^e(Z)$, curves of $\langle \rho | Z \rangle$ and $\rho^e(Z)$ are shown in figure 5 for simulations B and C. The precise magnitude of the heat release is not critical to the state relation (provided it is not unrealistically small); decreasing the heat release merely increases the approximately constant minimum density that prevails over much of the central part of the mixing layer. Qualitatively, there always is a central region of low density bounded by two interfaces with the dense fluid in the free streams.

In variable-density flows it can be useful to use Favre p.d.f.s (Bilger 1977),

$$\tilde{P}(Z) = \frac{1}{\bar{\rho}} \int \rho P(\rho, Z) \mathrm{d}\rho. \tag{4.1}$$

A consequence of the state relation for density is that, from (4.1),

$$\tilde{P}(Z) = \frac{\rho^e(Z)}{\bar{\rho}} P(Z). \tag{4.2}$$

It follows further that, for any random variable ψ,

$$\tilde{P}(Z, \psi) = \frac{\rho^e(Z)}{\bar{\rho}} P(Z, \psi), \tag{4.3}$$
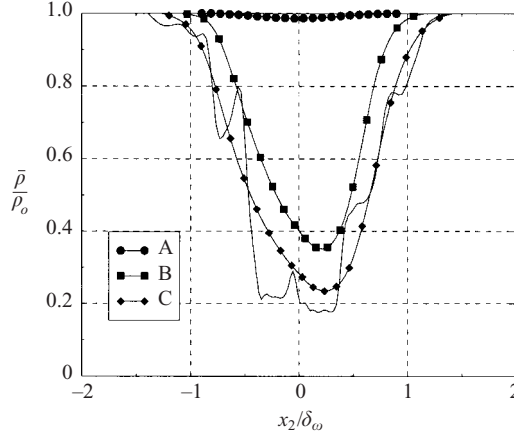
FIGURE 6. Average density profiles for different levels of heat release and an instantaneous profile for simulation C (thin line).

and so

$$\tilde{P}(\psi|Z) = P(\psi|Z), \qquad (4.4)$$

implying the equivalence of Z-conditioned Favre and Reynolds averages,

$$\widetilde{\langle\psi|Z\rangle} = \langle\psi|Z\rangle. \qquad (4.5)$$

In addition,

$$\langle\rho\psi|Z\rangle = \rho^e(Z)\langle\psi|Z\rangle. \qquad (4.6)$$

A number of implications thus arise when the state relation $\rho = \rho^e(Z)$ is a reasonable approximation.

5. Average flow statistics

A representative instantaneous density profile for simulation C, illustrating the typical non-monotonicity that results from turbulent eddy turnover, is shown in figure 6. The instantaneous and conditioned density variations are reflected in the average density profiles also shown in figure 6, taken at the end of the simulation in all the cases. Since the largest Reynolds number occurs at the end of the simulation, all subsequent results also are shown at the end of each DNS, unless otherwise stated. The large variations in the mean density associated with heat release are evident in figure 6, resulting in average maximum density ratios $\bar{\rho}_{min}/\bar{\rho}_{max}$ of 0.35 for case B and 0.23 for case C, compared with maximum instantaneous density ratios of $\rho_{min}/\rho_{max} = 0.29$ and $\rho_{min}/\rho_{max} = 0.18$, respectively. The effect of such large density changes on the turbulence evolution becomes clear upon examining the turbulent kinetic energy, turbulent dissipation, scalar variance and scalar dissipation.

Figure 7 shows profiles of both Reynolds-averaged and Favre-averaged (*a*) streamwise velocity, and (*b*) mixture fraction, across the shear layer for the highest level of heat release. Although there is little difference between Reynolds and Favre averaging here, the Reynolds-averaged profiles lie below the Favre-averaged profiles on the fuel side of the domain, $x_2/\delta_\omega \lesssim 0.25$, and above them on the oxidizer side, $x_2/\delta_\omega \gtrsim 0.25$. The differences between these curves can be traced to the definitions of
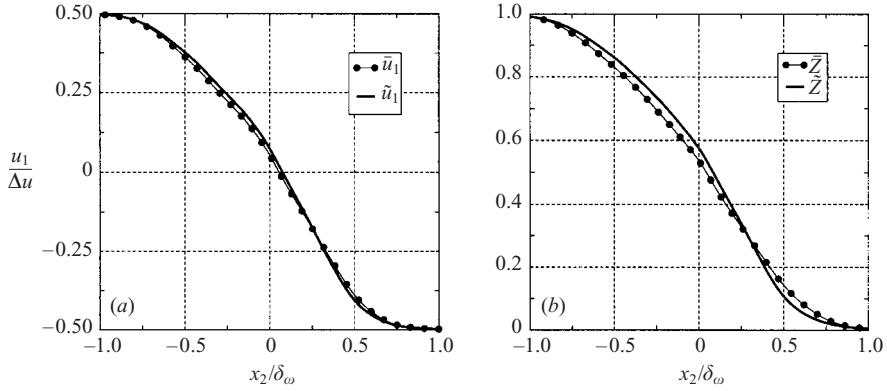
FIGURE 7. Reynolds and Favre mean profiles as functions of the normalized vertical coordinate at different levels of heat release for case C; (*a*) average streamwise velocity and (*b*) average mixture fraction.

the Favre and Reynolds averages, which result in

$$\tilde{u}_1 - \bar{u}_1 = \frac{\overline{\rho' u_1'}}{\bar{\rho}} \tag{5.1}$$

and

$$\tilde{Z} - \bar{Z} = \frac{\overline{\rho' Z'}}{\bar{\rho}}, \tag{5.2}$$

the cross-fluctuations on the right-hand sides being positively correlated on the fuel side and negatively correlated on the oxidizer side. This is understandable in that higher Z tends to be associated with higher ρ on the fuel side and with lower ρ on the oxidizer side. Similarly, u_1 is positive on the fuel side, where Z is larger, and negative on the oxidizer side, where Z is smaller (figure 1). As expected these effects are larger for Z than for u, because of the good state relation for ρ, just discussed, but not for u_1, and they increase in proportion to heat release, being absent in case A.

Since the constant velocity difference, Δu, is imposed in the shear layer, the turbulent kinetic energy, $\tilde{k}$, defined in (3.30) and Favre-averaged Reynolds stresses, $\widetilde{u_i'' u_j''}$, are expected to scale as Δu^2. Since the vorticity thickness, δ_ω, is a direct measurement of the mean velocity gradient across the shear layer, it serves to scale the x_2 dependence of $\tilde{k}$, while the momentum thickness,

$$\delta_\theta(t) = \frac{1}{\rho_o \Delta u^2} \int_{-\infty}^{\infty} \bar{\rho} \left(\frac{\Delta u}{2} - \tilde{u}_1 \right) \left(\frac{\Delta u}{2} + \tilde{u}_1 \right) \mathrm{d}x_2, \tag{5.3}$$

does not collapse the widths of profiles in the three cases and is not used further. Figure 8(*a*) shows the resulting normalized $\tilde{k}$ profiles for different levels of heat release, while figure 8(*b*) presents associated normalized $\tilde{\epsilon}$ profiles with the same scaling, where $\tilde{\epsilon}$ is defined in (3.31). These profiles exhibit almost identical shapes for the simulations with heat release, demonstrating the usefulness of the non-dimensionalization. With heat release, however, the $\tilde{k}$ levels are 30% below those without, and the $\tilde{\epsilon}$ levels are 40% below. The reduction in $\tilde{k}$ by heat release has already been observed in DNS calculations of shear layers with lower levels of heat release by McMurtry *et al.* (1989) and by Miller *et al.* (1994). This indicates that rather little heat release is needed to bring about this change, and the present results suggest that higher levels
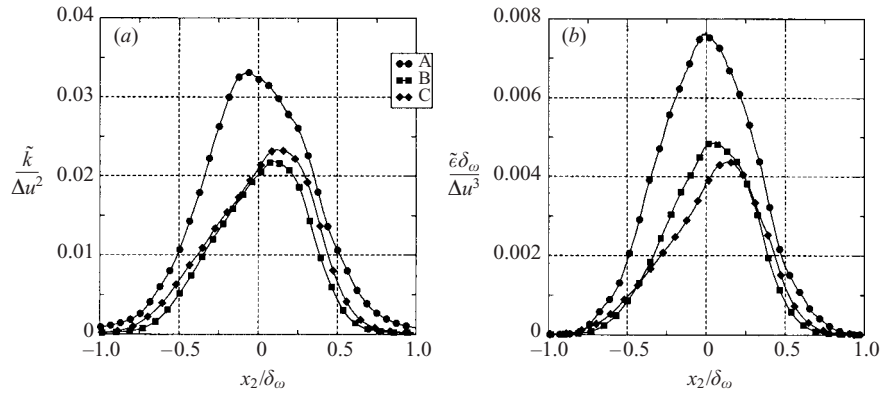
FIGURE 8. Turbulent kinetic energy (*a*) and dissipation (*b*) variations across the shear layer for three different levels of heat release (cases A, B and C).
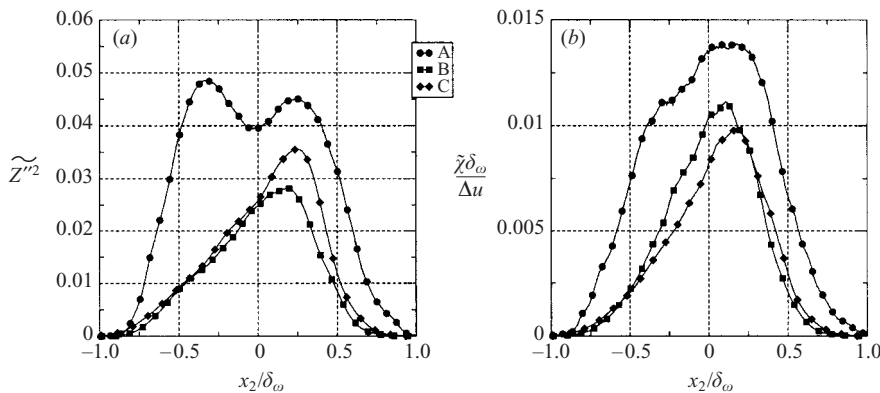

FIGURE 9. Scalar variance (*a*) and dissipation (*b*) variations across the shear layer for three different levels of heat release (case A, B and C).

of heat release have relatively little effect. While the overall widths of the profiles are approximately the same, the ones with heat release have a somewhat different shape, narrower in the central region. Figure 8 also shows that the heat release tends to shift the location of the peak generation of turbulent kinetic energy towards the side of the shear layer where the stoichiometric surface is (when $Z_s \neq 0.5$). This is a consequence of enhanced generation of turbulence through the strong density fluctuations in the vicinity of the reaction sheet.

Figure 9 shows the effects of heat release on the profiles of the scalar variance, $\widetilde{Z''^2}$, and $\tilde{\chi}$, with the same non-dimensionalization as employed in figure 8. Heat release has the same general effect on these profiles that was observed for the $\tilde{k}$ and $\tilde{\epsilon}$ profiles, that is narrowing the central region and lowering of the peak values. The locations of the peaks of $\widetilde{Z''^2}$ and $\tilde{\chi}$ also coincide approximately with those of $\tilde{k}$ and $\tilde{\epsilon}$, for the same reason. The reduction of the peak $\tilde{\chi}$ is less pronounced than that of $\tilde{\epsilon}$. Comparison of figure 8 with figure 9 indicates a larger reduction of the profile thickness with increasing heat release for the scalar quantities in comparison with the turbulence quantities. This implies that the scalar integral scale is reduced more than the velocity integral scale at the same heat-release level, consistent with effects on
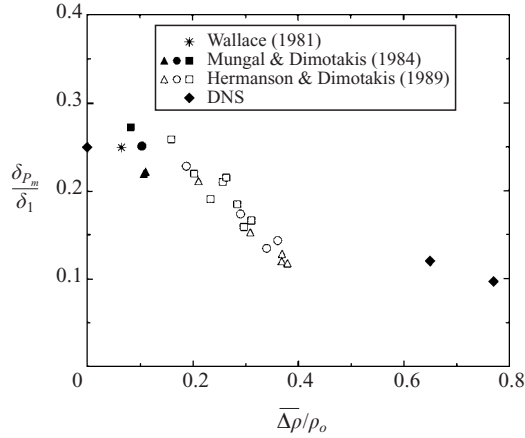
FIGURE 10. Effect of heat release on normalized product mass thickness.

ratios of time scales, discussed below. The smaller reduction of peak value coupled with the narrower peak for the scalar indicates that the effect of Q is approximately the same for the velocity and scalar quantities when integrated across the shear layer. Since without heat release (case A) the profiles in figures 8 and 9 statistically on the average must be symmetric about $x_2/\delta_\omega = 0$, the observed departures from this symmetry are reflective of the deviations of computed averages from the true expected values that are present in DNS because of finite statistical sample size.

The effect of Q on spectra of the velocity and scalar fields also is of interest, but differing Reynolds numbers for different values of Q in these simulations obscured possible influences of heat release. Spectra are therefore not shown here.

A measure of scalar mixing efficiency that has been found useful experimentally (Hermanson & Dimotakis 1989) is defined conceptually as

$$\delta_{P_m} = \int_{-\infty}^{\infty} \frac{\bar{\rho}\tilde{Y}_P}{\rho_o Y_P(Z_s)}\,\mathrm{d}x_2 \tag{5.4}$$

and has been called the product mass thickness. This thickness has been inferred from temperature measurements in spatially evolving planar shear layers and plotted, normalized by the 1% thickness based on the mean temperature profile, δ_1, as a function of a measure of heat release, $\overline{\Delta\rho}/\rho_o$, where $\overline{\Delta\rho}$ is ρ_o minus the minimum mean density seen in figure 6. In a self-similar evolving mixing layer δ_{P_m}/δ_1 is a constant which, in principle, could depend on heat release. Figure 10 shows the experimental data and the results of the three present simulations. Although temporally rather than spatially evolving, the simulations are seen to produce results that are in good agreement with experiment. They further support the conclusion that there is a systematic reduction in δ_{P_m}/δ_1 with increasing heat release, and they extend to higher heat release than the experiments, indicating a decrease from 0.25 with no heat release to 0.1 at large heat release.

6. Ratios of time scales

Turbulence time scales are readily extracted from the preceding results. A mechanical (large-eddy) time is

$$\tau_K = \tilde{k}/\tilde{\epsilon}, \tag{6.1}$$

and a corresponding scalar time scale is

$$\tau_Z = \widetilde{Z''^2}/\tilde{\chi}. \tag{6.2}$$

The ratio of the mechanical time scale to the scalar time scale is the time-scale ratio

$$r = \frac{\tau_K}{\tau_Z}, \tag{6.3}$$

which is often assumed to be unity in turbulence modelling (Jones 1994). There are uncertainties concerning possible dependences of r on Q and Re. In the present simulations, in principle r may vary with x_2, and an average ratio across the shear layer may be defined as

$$r_{avg}(t) = \frac{1}{\delta_\omega(t)} \int_{-\delta_\omega/2}^{\delta_\omega/2} r(x_2, t) \, dx_2. \tag{6.4}$$

Table 3 lists both r_{avg} and the peak value of r. All values of r were found to be within 20% of r_{avg}, and, in particular, no systematic dependence of r on x_2 was found to exist, there being only gradual fluctuations of r with x_2, at about the 20% level. The only clear systematic dependence of any parameter on r is that of the heat release Q. For $Q = 0$, it was observed that $r \approx 1.2$, while in the two simulations with heat release, r was larger by about 40%, $r \approx 1.6$. It may therefore be concluded that a relatively small amount of heat release (decreasing the density by something like a factor of two) appreciably increases the ratio r, but additional heat release then has a negligible effect.

There are somewhat conflicting results in the literature concerning the effect of Re on r. Some information related to this can be extracted from the present simulations. The vorticity thickness δ_ω increases slowly with time in the simulations, resulting in a slow increase of Re. The growth, $d\delta_\omega/dt \approx 0.1\Delta u$, is slow enough that time-dependent effects are unlikely to be important, but Re increases by a factor of about 2.5 from the beginning to the end of the simulations. Results, such as those in table 3, where the r values are averages over the last third, mainly pertain to conditions towards the end of the simulations, and correspond to the largest Re. The value of r_m was calculated as a function of time during these simulations, to explore possible influences of Re. A tendency for r_m to increase with Re was evident, but that tendency was very small. With heat release, r_m initially increased from about 1.4 to about 1.6 then remained fairly constant as Re increased further, while for $Q = 0$ there seemed to be a gradual variation from slightly less than 1.2 to about 1.3, the value in table 3. The results thus suggest that the Reynolds numbers of the simulations were large enough that the effect of Re on r was very small.

Warhaft (2000) measured r in decaying grid turbulence with a mean scalar gradient and found an asymptotic value of 1.5, very close to our values. On the other hand, Tavoularis & Corrsin (1981) report values between 2.17 and 3.12 for homogeneous sheared turbulence. It is very difficult to measure r accurately in turbulent combustion, and Chen & Mansour (1997) estimate values between 0.2 and 1.46 in turbulent reacting hydrogen jets, the largest of which agrees with our results. Computationally, Spalding (1971) was able to calculate the mean scalar evolution in a round turbulent free jet with $r \approx 1.8$ in $k - \epsilon$ modelling. More recent modelling studies, employing values not too different from ours, include the works of Newman, Launder & Lumley (1981), Shih & Lumley (1986), Shih, Lumley & Janicka (1987), Hirai & Takagi (1991) and Gharbi *et al.* (1996). Overholt & Pope (1996) report DNS of forced isotropic turbulence with a passive-scalar gradient, obtaining a systematic increase of r with
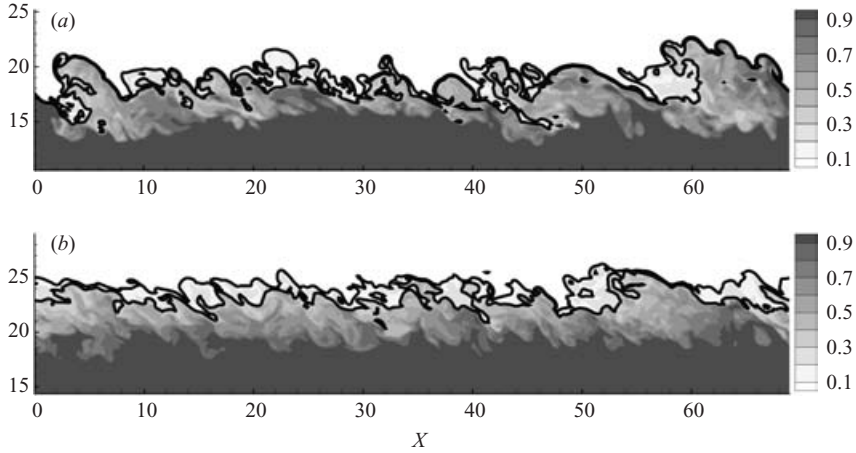
FIGURE 11. Scalar contour plots at times when the vorticity thicknesses are approximately equal for (*a*) case A, $Re_{\lambda,m} = 130$ and (*b*) case B, $Re_{\lambda,m} = 95$. Thick lines are $Z = Z_s \pm 0.1$.

Re, from 1.8 to 3.0. This result disagrees with ours, possibly because the forcing to achieve stationarity contributes to the turbulent kinetic energy in a manner different from natural turbulent shear flows.

7. Scalar p.d.f.s

Probability-density functions of the mixture fraction help to show the extent of mixing to the molecular level. Delta functions at $Z = 0$ and $Z = 1$ theoretically identify unmixed fluid and may be said to mark intermittency of the scalar field. Like experiments, the simulations smear delta functions into continuous divergences.

An idea of how heat release modifies the p.d.f.s can be obtained by studying the two representative instantaneous vertical cuts of Z isopleths across the shear layer shown in figure 11, where the horizontal and vertical axis are the x_1 and x_2 coordinates of figure 1. The times of these two cuts were selected to correspond to approximately the same δ_ω for the simulations without heat release at the top and that with heat release at the bottom. There are significant differences in the shapes of the boundaries of the two darkest regions, for example, as well as in the shapes of the boundaries of the two lightest regions. In figure 11(*a*), these boundaries show undulations of much larger vertical extent than in figure 11(*b*). This difference is reflected in similar differences in the corresponding boundaries seen in figure 3 for temperature and density. It implies a much greater degree of external scalar intermittency in the simulation without heat release. In the extreme, without heat release there are instances in which the darkest and lightest regions almost border each other, as at the far left of figure 11(*a*), but this never occurs with heat release. The comparatively large-scale organization that occurs without heat release, with large eddies separated by these mixing regions, is consistent with the earlier DNS results of Rogers & Moser (1994). The differences may be related to the different linear stability properties of the shear layers (Shin & Ferziger 1991; Planché 1992; Day, Mansour & Reynolds 2001).

Figure 12 compares scalar p.d.f.s for late-time simulations with heat release (*b*) and without (*a*). The statistics are obtained from the DNS results in the (x_1, x_3)-plane (by constructing histograms with 64 bins, giving sufficient resolution without excessive fluctuations) at five different values of x_2, namely those at which $\bar{Z}$ takes the values
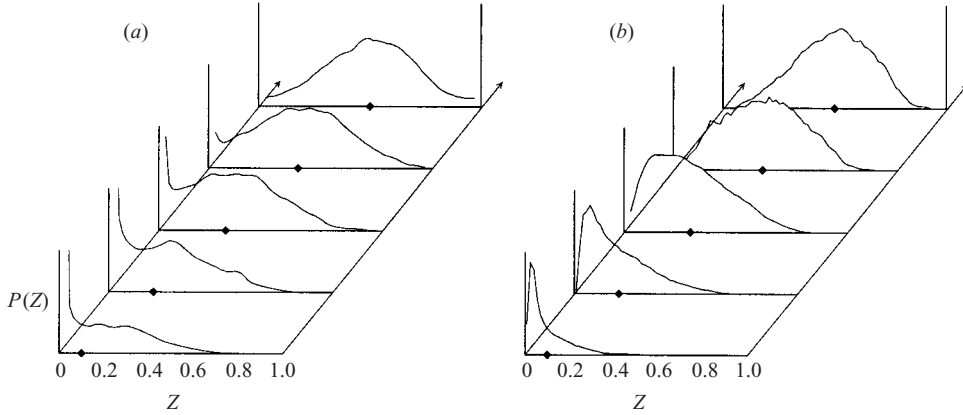
FIGURE 12. Scalar p.d.f. for simulations A (*a*) and C (*b*) at late time. From bottom to top, values of x_2 are those at which $\bar{Z} = 0.1, 0.2, 0.3, 0.4$ and 0.5. Symbols correspond to mean values.
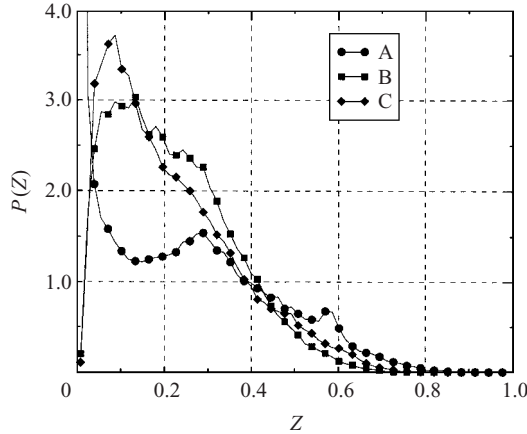

FIGURE 13. Scalar p.d.f. at the value of x_2 where $\bar{Z} = Z_s = 0.2$ for three different levels of heat release (cases A, B and C).

0.1 to 0.5. Not shown are corresponding results for $\bar{Z}$ from 0.6 to 0.9, but without heat release they are symmetrical (as they must be), the divergences seen at $Z = 0$ now appearing at $Z = 1$. With heat release they are qualitatively similar but quantitatively different, the main difference being that they are slightly narrower at the intermediate values of $\bar{Z}$ for $\bar{Z} > 0.5$. Heat-release results are shown only for simulation C because those for B are qualitatively the same.

The main difference between the two sets of results in figure 12 is the evident intermittency without heat release for $\bar{Z} \neq 0.5$, a behaviour that is not seen with heat release. Unlike the sequence in figure 12(*b*), that in (*a*) is distinctly bimodal at $\bar{Z}$ of 0.2 and 0.3, with both the mixed-fluid peak and the divergent intermittency peak at $Z = 0$. The comparisons can be seen more accurately in figure 13, where the results in figure 12 at $\bar{Z} = 0.2 = Z_s$ are plotted on the same scale, along with the corresponding results of the other heat-release DNS. Clearly, the implied delta function at $Z = 0$ is present in figure 13 only for case A ($Q = 0$). With heat release,
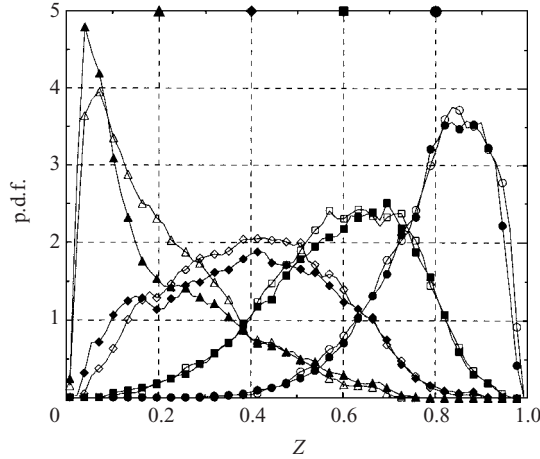
FIGURE 14. Scalar Reynolds and Favre p.d.f.s for simulation C at late time, $Re_{\lambda,m} \sim 80$. Circles: $\bar{Z} = \tilde{Z} = 0.8$, squares: $\bar{Z} = \tilde{Z} = 0.6$, diamonds: $\bar{Z} = \tilde{Z} = 0.4$ and triangles: $\bar{Z} = \tilde{Z} = 0.2$. Filled symbols correspond to Favre p.d.f.s and open symbols to Reynolds p.d.f.s.

the mode in figure 13 does not coincide exactly with the mean, it being closer to $Z = 0.1$ than to $Z = 0.2$, and increasing Q is seen to raise and sharpen the peak of $P(Z)$.

The p.d.f.s with peaks that nearly coincide with the mean and that move to higher Z as $\bar{Z}$ increases across the mixing layer have been called 'marching' (Mungal & Dimotakis 1984) in that they march uniformly across the shear layer with $\bar{Z}$, while those having modes that do not line up with the mean are 'non-marching'. In this terminology, the p.d.f.s for $Q = 0$ are non-marching, while those with $Q \neq 0$ are more nearly marching, although not exactly so, especially at the extremes of $\bar{Z}$. Non-marching p.d.f.s are characteristic of flows with external intermittency, which exhibit large-eddy engulfment of fluid then small-scale mixing. The results obtained here are consistent with those of previous computations (Rogers & Moser 1994) and experiments (Mungal & Dimotakis 1984; Clemens & Mungal 1995; Clemens & Paul 1995; Starner *et al.* 1997; Miller, Bowman & Mungal 1998; Barlow *et al.* 2000) in indicating that heat release suppresses intermittency and promotes marching p.d.f.s. With values of Q representative of turbulent combustion, cross-stream structures do not penetrate the low-density region and therefore cannot span the entire width of the shear layer.

Both Reynolds and Favre (equation (4.1)) p.d.f.s can be calculated from the present DNS and compared. Figure 14 shows such a comparison for case C, at values of x_2 corresponding to four different values of the mean. The means taken here for $P(Z)$ are $\bar{Z}$, while those for $\tilde{P}(Z)$ are $\tilde{Z}$, so that they actually correspond to slightly different values of x_2; if this is not done, the same values of x_2 being used, then the Reynolds and Favre curves are shifted slightly with respect to each other because of the different values of the two means. Figure 14 shows that $P(Z)$ and $\tilde{P}(Z)$ are very nearly the same. That they exhibit the same features is consistent with experimental results in hydrogen–air jet flames by Kennedy & Kent (1978). The only significant difference between Favre and Reynolds p.d.f.s of figure 14 occurs at the average value of 0.2, which equals Z_s. It is understandable that the largest differences occur in the
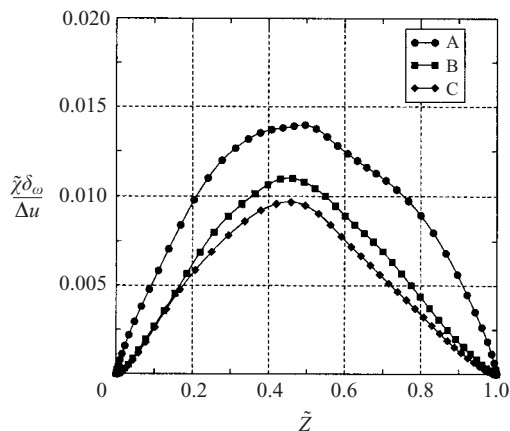
FIGURE 15. Replot of figure 9(b) in terms of the normalized unconditional average scalar dissipation as a function of the Favre mean scalar $\tilde{Z}$ for simulations A, B and C.

vicinity of the flame sheet because this is where the largest density fluctuations will occur. The Favre p.d.f. there is seen to be narrower and more sharply peaked than the Reynolds p.d.f., in agreement with the experimental observations of Kennedy & Kent (1978). The asymmetry of the four curves, those for 0.4 differing from those for 0.6 and 0.2 differing from 0.8, is associated with the asymmetry of the density profiles seen in figure 5.

8. Conditional scalar dissipation

As indicated in the introduction, the conditionally averaged scalar dissipation, $\langle \chi | Z \rangle$ of (1.2), is of greater interest than the profiles of the unconditioned average scalar dissipation shown in figure 9(b). This is because of the relevance of the former to the averaged reaction rate and its appearance in various modelling approaches. Statistics of the dependence of χ on Z are in general of great interest in turbulent combustion. Replotting figure 9(b) in terms of the averaged mixture fraction instead of x_2/δ_ω is indicative but misleading. Figure 15 is a Favre version of such a plot. Since the curve for $Q = 0$ must be symmetrical about $\tilde{Z} = 0.5$, the departures from this symmetry seen in the figure are indicative of the magnitude of deviations from the expected value in the computed DNS averages; the small hump on the right in this figure corresponds to the hump on the left in figure 9(b). The three similar bell-shaped curves in figure 15 look very much like those of χ as a function of Z in steady laminar counterflow mixing, thereby suggesting a possible ensemble of quasi-steady laminar counterflow diffusion flamelets, with the corresponding dependence $\chi(Z)$ applying locally everywhere on a space–time-resolved basis. This view, however, is entirely false, as study of the conditional dissipation will reveal.

The conditional average, $\langle \chi | Z \rangle$, depends on x_2 in these flows. Although it is possible, in principle, to calculate this directly from the DNS data, the need to address the two variables, χ and Z, degrades the statistics. Calculations were made using data at ten different instants of time in the late-time evolution to obtain ensemble averages with reduced fluctuations, and the results suggested that the dependence on x_2 was not large, especially if $Q \neq 0$. The dependence of $\langle \chi | Z \rangle$ on x_2 was largest for $Q = 0$ and mainly for the more extreme values of Z ($Z < 0.2$ and $Z > 0.8$). It proved to be easier to make accurate calculations of the product $\langle \chi | Z \rangle P(Z)$ at different x_2-planes
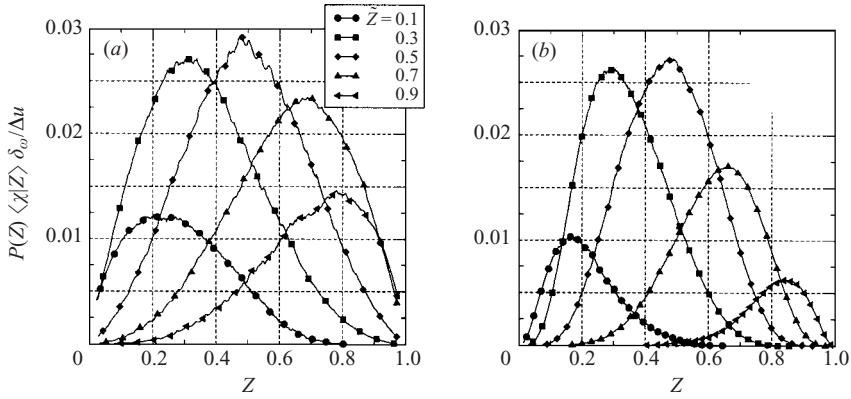
FIGURE 16. Profiles of the normalized product $P(Z)\langle\chi|Z\rangle$ for (*a*) case A, and (*b*) case C. The different curves correspond to the different x_2-planes where the mean scalar is 0.1, 0.3, 0.5, 0.7 and 0.9.
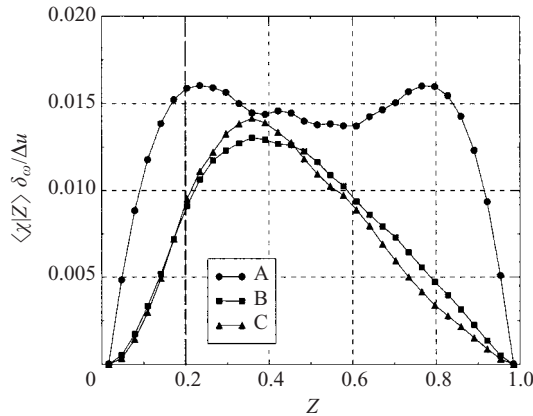

FIGURE 17. Normalized conditional average scalar dissipation for simulations A, B and C.

because the additional factor $P(Z)$ suppresses rare events with large fluctuations. This product, $\int_0^\infty \chi P(\chi, Z)\mathrm{d}\chi$ according to (1.2), shown in figure 16 for cases A and C, at five different x_2-planes corresponding to the five different values of $\bar{Z}$ listed, also appears directly in the average reaction rate and has been used specifically in modelling (Kollmann & Janicka 1982), so that it is of interest in itself. Accuracy of the curves in figure 16 may be judged from the fact that for $Q = 0$ (figure 16*a*) the curves for $\bar{Z} = 0.1$ and $\bar{Z} = 0.9$ must be situated symmetrically about $Z = 0.5$, as must the curves for $\bar{Z} = 0.3$ and $\bar{Z} = 0.7$. Division of the curves in figure 16 by the $P(Z)$ curves of figure 12 generates curves of $\langle\chi|Z\rangle$, which by this alternative method also are found not to depend too strongly on x_2. The relative weak x_2 dependence makes averages taken over the entire computational volume relevant, and such averages have greatly reduced statistical scatter. For this reason they have also been used in measurements of turbulent hydrogen jet flames (Chen & Mansour 1997), where experimental evidence for the weak dependence on position was obtained. Neglect of the x_2 dependence has also been useful in modelling (Li & Bilger 1993).

Figure 17 shows $\langle\chi|Z\rangle$ averaged over the total volume and over about 10 different instants of time for all three simulations at late time. The normalizing factor $\delta_\omega/\Delta u$
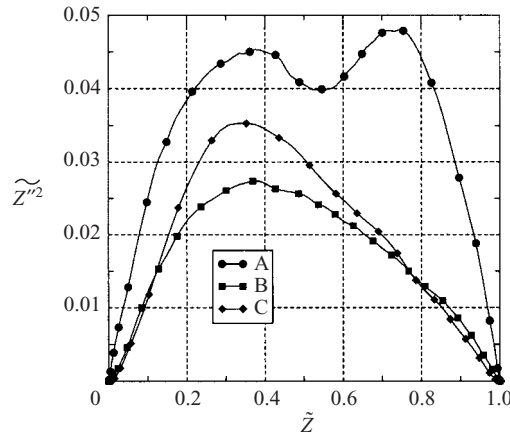
FIGURE 18. Replot of figure 9(*a*) in terms of the unconditional scalar variance as a function of the Favre average scalar (cases A, B and C).

helps to remove any Re_ω dependence. The difference between figure 17 and figure 15 is striking. The dissipation curves in figure 17 are shaped much more like the variance curves in figure 9(*a*) than the dissipation curves in figure 15, as may be seen by replotting the variance as a function of Z instead of x_2/δ_ω. Figure 18 directly compares the corresponding Favre version of figure 9(*a*) for cases A, B and C, the results being essentially the same as they would have been if the Reynolds version had been used instead. The most notable observation is the substantial effect of heat release on these curves. The double hump in the variance for $Q = 0$ in figure 9(*a*) is well established, not only here but also in other work (Fiedler 1974; Miller *et al.* 1994), and it has been interpreted in terms of scalar intermittency as resulting from engulfment being more dominant near the edges of the mixing layer, resulting in somewhat larger scalar fluctuations there. The heat release eliminates this effect by establishing the low-density central region and also removes the symmetry about $\tilde{Z} = 0.5$ by shifting the variance peak towards the mean stoichiometric surface, where fluctuations are largest. The tracking of these position-dependent phenomena by the volume-averaged conditional mean dissipation, quite a different statistical quantity, must be a reflection of the conditional mean dissipation being largest for values of mixture fraction about which the variance is largest, irrespective of where these values may occur in the field. The difference between the two curves with $Q \neq 0$ in figure 17 is not statistically significant; a relatively small amount of heat release completely removes the double-hump character, eliminating the tendency towards achieving nearly constant $\langle \chi | Z \rangle$ over most Z ($0.2 \lesssim Z \lesssim 0.8$) and generating instead a bell-shaped curve with peaks skewed towards (but not reaching) the stoichiometric value Z_s. The skewing is more pronounced for $\langle \chi | Z \rangle$ than for $\widetilde{Z''^2}$, peaks of the conditional quantity being somewhat farther from 0.5. The large effect of Q on $\langle \chi | Z \rangle$ is removed when this quantity is multiplied by $P(Z)$ (figure 16), which suggests that it may be easier to model the product directly.

Modelling can be facilitated if $\langle \chi | Z \rangle$ is nearly independent of Z for most of the range of Z, as it is in figure 17 for $Q = 0$. This enables the approximation $\langle \chi | Z \rangle = \bar{\chi}$ to be introduced, an approximation that would apply if χ and Z were statistically independent. According to figure 17, such statistical independence is inaccurate for $Q \neq 0$, but it might be a reasonable approximation for $Q = 0$, even though the
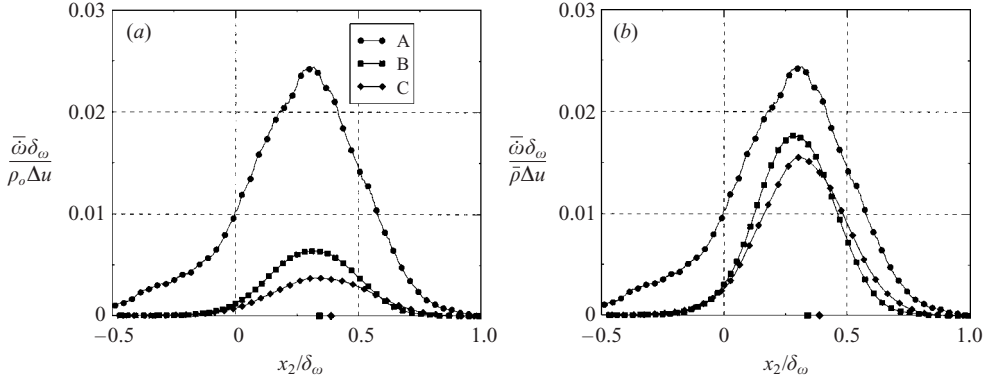
FIGURE 19. Effect of heat release on average reaction rate profiles: (a) average reaction rate, (b) average reaction rate normalized by mean density.

boundary conditions imposed on the problem require it to fail as Z approaches 0 or 1, where χ vanishes. There are corresponding inadequacies in neglecting the χ, Z correlation in homogeneous turbulence, where, for example, it precludes relaxation of an initially double-delta Z field to its ultimate Gaussian, at which the correlation vanishes (Eswaran & Pope 1988; Valiño, Dopazo & Ros 1994). The $\langle\chi|Z\rangle$ profiles in homogeneous turbulence with $Q \neq 0$ from the DNS of Mell et al. (1994) are very similar to ours. The homogeneous-turbulence DNS of Mahalingam et al. (1995), in which μ increased with T, showed substantial reduction in the magnitude of $\langle\chi|Z\rangle$ with heat release, much greater than in figure 17 (where μ is constant), probably because of consequent reduced intensities $\widetilde{Z''^2}$, that in our case do not decay. Experimental profiles of $\langle\chi|Z\rangle$ in turbulent hydrogen jet flames (Chen & Mansour 1997) closely resemble ours, although a dip in $\langle\chi|Z\rangle$ at $Z = Z_s$ is reported, which is not observed in our simulation. Measurements of Starner et al. (1997) on diluted methane and hydrogen jet flames show shapes of $\langle\chi|Z\rangle$ that are similar to ours near the external shear layer. The results in figure 17 thus have some independent computational and experimental support while indicating that with representative heat release the statistical dependence of χ on Z needs to be taken into account for accurate modelling.

It is known (Bilger 1980; Williams 1985) that in the Burke–Schumann approximation the average reaction rate when expressed in mass per unit volume per unit time is

$$\overline{\omega} \propto \rho^e(Z_s)\langle\chi|Z_s\rangle P(Z_s), \tag{8.1}$$

where the constant of proportionality depends on the chemical species considered. The characteristic average reciprocal time for the reaction, $\overline{\omega}/\rho^e(Z_s)$, can thus readily be read from figure 16 at $Z = Z_s$. Without heat release, the DNS results are independent of Z_s, and therefore figure 16(a) can be viewed as a graph of this characteristic time as a function of Z_s for various x_2-planes. Although this is not true for figure 16(b), that figure still provides an indication of how this time would vary with Z_s in different planes when $Q \neq 0$; there is not a great deal of differences between the two figures. Figure 19 shows profiles of the non-dimensional average reaction rates $\overline{\omega}\delta_\omega/(\rho_o\Delta u)$ and $\overline{\omega}\delta_\omega/(\bar{\rho}\Delta u)$ as functions of x_2/δ_ω, obtained from the DNS (with $Z_s = 0.2$). The points at the bottom mark the position x_2/δ_ω at which $\bar{Z} = Z_s$. The curves are not centred in the middle of the mixing layer but instead move towards the position
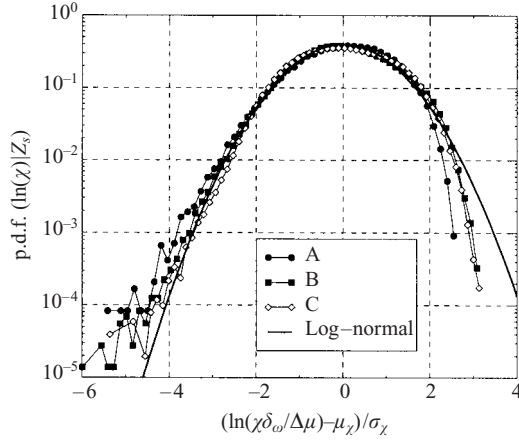
FIGURE 20. The p.d.f. of the normalized conditional scalar dissipation at Z_s for different levels of heat release. Thick line corresponds to fitted log-normal distributions.

of the average stoichiometric mixture fraction, peaking near but not exactly at that position; they are shifted slightly towards the centre of the mixing layer by amounts that increase with increasing Q. The density reduction for $Q \neq 0$ is seen in figure 19(a) to greatly reduce the average mass rate of consumption of reactants. Dividing by the local average density, as in figure 19(b), is seen to largely offset this reduction, although the rate is still about 40% lower at the largest value of Q than at $Q = 0$. This additional effect is associated with the influence of the density change on the turbulent mixing. Since the profiles in figure 19(b) are also appreciably narrower for $Q \neq 0$ than for $Q = 0$, the reduction in the overall reaction rate, integrated across the shear layer, caused by the influence of the density decrease on scalar mixing, is substantial.

Besides the conditional means, the p.d.f. of χ conditioned on Z is of interest. As seen in (1.2), this is $P(\chi|Z) = P(\chi, Z)/P(Z)$. The p.d.f.s for χ often are approximated as log-normal. Such an approximation for χ conditioned on Z being stoichiometric is

$$P(\ln(\chi \delta_\omega/\Delta u)|Z_s) = \frac{1}{\sqrt{2\pi\sigma_\chi^2}} \exp\left(-\frac{(\ln(\chi \delta_\omega/\Delta u) - \mu_\chi)^2}{2\sigma_\chi^2}\right). \quad (8.2)$$

A measure of the departure from log normality is the skewness factor

$$S_\chi = \frac{\overline{(\ln \chi - \langle \ln \chi \rangle)^3}}{\sigma_\chi^{3/2}}. \quad (8.3)$$

Figure 20 tests this log normality for all three simulations at late time, employing DNS data taken over the entire computational domain.

The values of the mean μ_χ, the standard deviation σ_χ and the skewness S_χ are listed in table 4 for all three cases. Figure 20 shows log normality to be a reasonable approximation. This conclusion has also been obtained experimentally (Nandula *et al.* 1994; Chen & Mansour 1997; Starner *et al.* 1997), the latter also indicating a negative skewness factor, similar to the present results. Measurements and computations like this pertaining to the conditional p.d.f. are relative sparse; it is well established that the unconditional p.d.f. is closely log normal (Kerstein & Ashurst 1984; Anselmet & Antonia 1985; Eswaran & Pope 1988; Pumir 1994; Overholt & Pope 1996).

Case	Q	μ_χ	σ_χ	S_k
A	0.0	-5.323	1.716	-0.329
B	3.73	-6.165	1.710	-0.025
C	7.46	-6.021	1.677	-0.027

TABLE 4. Mean, standard deviation and skewness factor associated with the p.d.f. of $\ln(\chi\delta_\omega/\Delta u)$, conditioned at $Z = Z_s = 0.2$ for different levels of heat release.
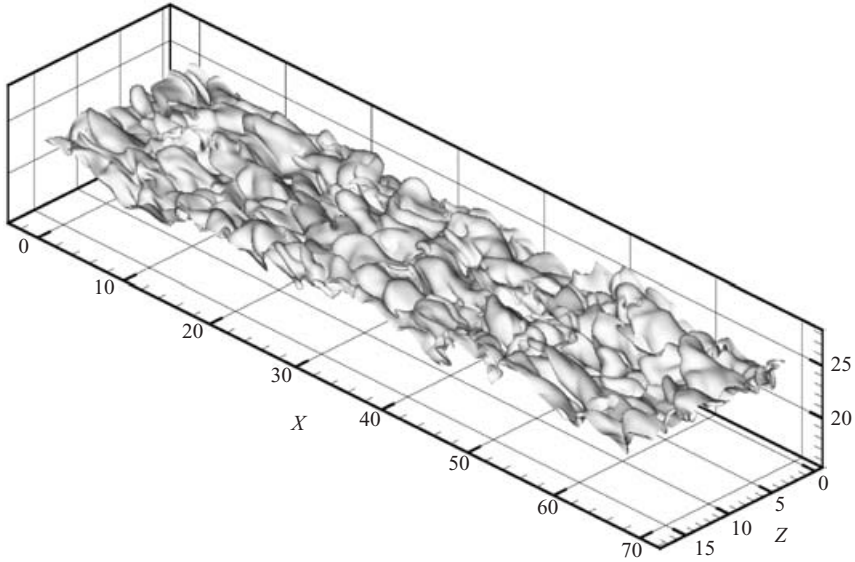

FIGURE 21. Scalar isocontour at $Z = Z_s$ for simulation C at late time.

The more negative values of μ_χ in table 4 for $Q \neq 0$ reflect the correspondingly lower averages seen in figure 17. The standard deviations, however, are seen in table 4 to be essentially independent of Q. The skewness factor in table 4 is larger in magnitude by more than a factor of 10 for $Q = 0$ than for $Q \neq 0$, this difference also being visible in figure 20. In all cases, however, log normality begins to fail in the tails (figure 20). In summary, effects of heat release on the conditional p.d.f. of χ are noticeable but not large.

The conditional scalar dissipation is related to the thickness of the zone about $Z = Z_s$ in which molecular mixing and associated chemistry may occur. Roughly speaking, this thickness is of order $Z_s/|\nabla Z|$, the gradient being conditioned on $Z = Z_s$ Williams (1975); Vervisch & Poinsot (1998), and therefore an associated characteristic length may be defined as $l = Z_s\sqrt{2D/\chi}$, with D and χ correspondingly conditioned. Since heat release increases this D and decreases this χ (figure 17), it increases l, but it otherwise has little effect on the statistics of l, according to the results just described. The increase of l is visually apparent in figure 11, where contours at $Z = Z_s \pm 0.1$ have been thickened. Although there are large fluctuations, the average distance between these contours is larger in figure 11(b). A three-dimensional rendering of the stoichiometric surface in case C is given in figure 21, and a closeup of a section of figure 21, showing grid sizes employed, is shown in figure 22. The following sections
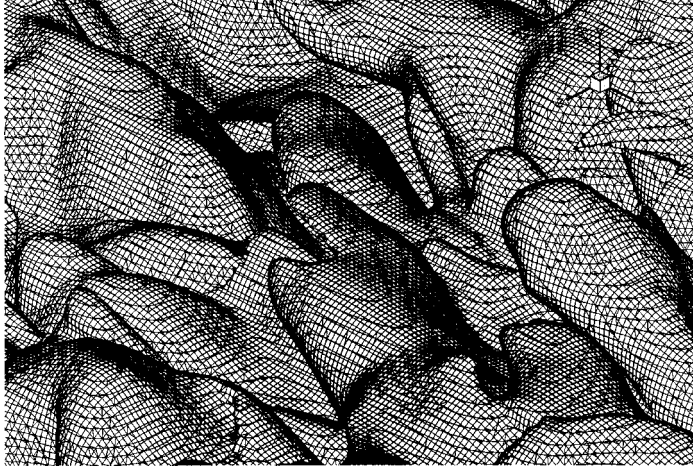
FIGURE 22. Zoom of the scalar isocontour at $Z = Z_s$ for simulation C at late time with corresponding mesh.

address in greater detail the structures of the Z and χ fields in the vicinity of this surface.

9. Statistical aspects of the stoichiometric surfaces and their vicinity

The topology of isoscalar surfaces is central to the validity of assumptions underlying modelling of non-premixed turbulent combustion. This is especially true for flamelet approaches that rely on expansions about $Z = Z_s$, but it also applies to CMC and p.d.f. approaches that deal with averages of χ conditioned on Z. Statistical aspects beyond those addressed in the preceding section have a bearing on this topology.

The simplest conceivable configuration is that of a planar stagnant molecular mixing layer, in which isoscalar surfaces are parallel planes, and $\sqrt{D/\chi}$ is constant everywhere. Since this uniformity of $|\nabla Z|$ from $Z = 0$ to $Z = 1$ is unrealistic in turbulence, steady counterflow laminar flamelet models have been considered, which maintain parallel planar isoscalar surfaces but have $|\nabla Z|$ varying smoothly from zero at $Z = 0$ or $Z = 1$ to a maximum near $Z = 0.5$. In each instantaneous realization these models have profiles that resemble those of the averages seen in figure 15 in Z-space and in figure 9(b) in physical space. Turbulence, however, generates much more complex topology for isoscalar surfaces, causing them to be non-planar and time-dependent, a fact that is responsible for the known limitations of steady laminar flamelet models, including those that take into account the linear variation of χ with Z near $Z = Z_s$. Turbulence can generate more than mild wrinkles in curves like those of figure 15 on *space–time-resolved* bases. Ridges can develop, with $|\nabla Z|$ achieving minima along certain surfaces, as well as zero-gradient points, where $\chi = 0$ (Gibson 1968). The wrinkles readily produce maxima and minima in instantaneous plots of χ as a function of Z along paths in the direction of ∇Z, and the minima descend to $\chi = 0$ at zero-gradient points. Since $\chi \geqslant 0$, such plots must in fact end when $\chi = 0$, turning back on themselves in at least one other maximum-gradient direction, at maximum and minimum values of Z different from 1 or 0, unless the zero-gradient point has an inflection type of behaviour instead of being a local absolute extremum.

These complexities deserve consideration in modelling and are being addressed by Peters & Trouillet (2002).

A first step in this direction is to study in greater detail the local behaviour of the Z and χ fields in the vicinity of isoscalar surfaces. Let y be the distance in the direction normal to the surface $Z = Z_s$, with $y > 0$ for $Z > Z_s$ and $y < 0$ for $Z < Z_s$. A Taylor expansion to second order in y then is

$$Z(y) = Z_s + a_1 y + a_2 y^2 + O\{y^3\}, \tag{9.1}$$

where

$$a_1 = \sqrt{\left(\frac{\partial Z}{\partial x_i}\right)^2} \tag{9.2}$$

and

$$a_2 = \frac{1}{2}\frac{\partial^2 Z}{\partial x_i \partial x_j} n_i n_j, \tag{9.3}$$

in which

$$n_i = \frac{1}{a_1}\frac{\partial Z}{\partial x_i} \tag{9.4}$$

is the ith component of a unit vector normal to the surface. All partial derivatives here are evaluated at the point where $Z = Z_s$. The second coefficient, a_2, differs from the curvature of the isoscalar surface $Z = Z_s$ itself, which is

$$\frac{\partial n_i}{\partial x_i} = \frac{1}{a_1}\left(\frac{\partial^2 Z}{\partial x_i^2} - n_i n_j \frac{\partial^2 Z}{\partial x_i \partial x_j}\right). \tag{9.5}$$

Both a_1 and a_2 are random variables in a turbulent flow. Since $\chi = 2Da_1^2$, there have, in effect, been numerous statistical studies of a_1, but a_2 has been relatively neglected. The expansion of χ about $Z = Z_s$, however, depends on a_2. To first order in $(Z - Z_s)$,

$$\chi = \chi_s + \left.\frac{d\chi}{dZ}\right|_{Z=Z_s} (Z - Z_s) + O\{(Z - Z_s)^2\}, \tag{9.6}$$

where

$$\left.\frac{d\chi}{dZ}\right|_{Z=Z_s} = 4D\frac{d^2 Z}{dy^2} + 2\frac{dD}{dZ}\left(\frac{dZ}{dy}\right)^2 = 8Da_2 + 2\frac{dD}{dZ}a_1^2, \tag{9.7}$$

the last term of which may be neglected because D typically reaches a maximum very near $Z = Z_s$. The good approximation

$$a_2 = \frac{1}{8D_s}\left.\frac{d\chi}{dZ}\right|_{Z=Z_s} \tag{9.8}$$

thus relates a_2 to the slope of the curve of χ as a function of Z at $Z = Z_s$. Since, according to (9.8), stagnant mixing-layer flamelet models have $a_2 = 0$, while steady counterflow laminar flamelet models with $Z_s < 0.5$ have $a_2 > 0$, the statistics of a_2 pertains to the potential applicability of these models.
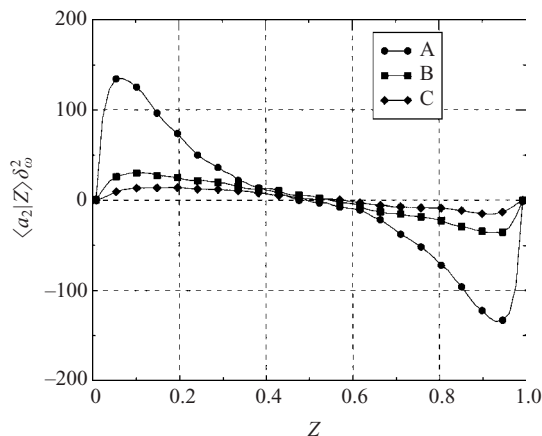
FIGURE 23. Conditional average of a_2 for different levels of heat release normalized with vorticity thickness.

Another reason for interest in a_2 is its relevance to limitations on the use of the characteristic length

$$l = Z_s \sqrt{\frac{2D_s}{\chi_s}} = \frac{Z_s}{a_1} \qquad (9.9)$$

identified at the end of the preceding section. This length defines the characteristic distance over which Z varies by a fractional amount of order unity only when the quadratic term in (9.1) is small compared with the linear term. This condition breaks down when $|y|$ becomes of order

$$d = \frac{a_1}{|a_2|}. \qquad (9.10)$$

The departure of Z from Z_s at this limit is

$$\Delta Z = Z_s \frac{d}{l} = a_1 d = \frac{a_1^2}{|a_2|}, \qquad (9.11)$$

which may be called the limiting scalar deviation in that Z ceases to vary linearly with distance y for distances beyond the value at which this deviation occurs. It thus is a measure of the amplitude of wrinkles of curves of Z as a function of distance normal to isoscalar surfaces, and we shall refer to d as a wrinkling length scale, or simply a wrinkle length. This limiting deviation and the associated limiting length, d, which is the characteristic linear dimension or length of such wrinkles, are random variables having statistics determined by those of a_1 and a_2. The statistics of a_1 and a_2, conditioned on $Z = Z_s$, thus have a bearing on a number of questions.

Graphs of the conditional average of χ as a function of Z have been shown in figure 17. These averages are basically equivalent to conditioned averages of a_1. Figure 23 shows corresponding graphs of conditional averages of a_2. For $Q = 0$ they are antisymmetric about $Z = 0.5$, as they must be (see (9.8), for example). They are also very nearly antisymmetric for $Q \neq 0$, suggesting that, although the dynamics correspond to $Z_s = 0.2$ in these cases, contrary to figure 17 for a_1, the asymmetry of the density field has little effect on a_2, thereby allowing any value of Z to be interpreted as Z_s. The density change has little effect on $\langle a_2 | Z \rangle$ for $0.3 \leqslant Z \leqslant 0.7$, but there are noticeable influences in the extremes representative of hydrocarbon–air
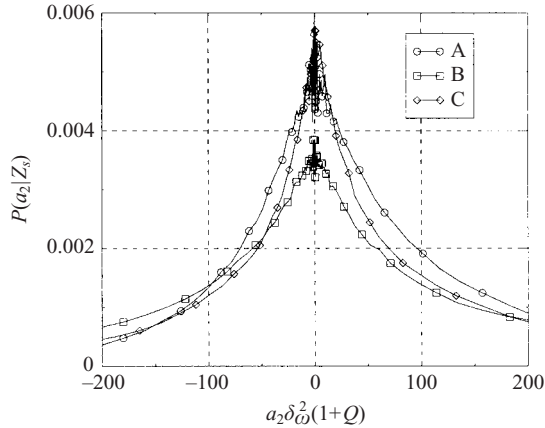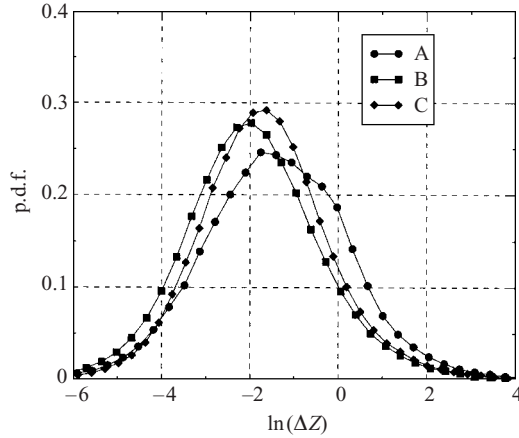
FIGURE 24. Conditional p.d.f. of a_2 at the stoichiometric surface for different levels of heat release.

combustion. The conditioned means all peak near $Z = 0.1$, but the peak for $Q = 0$ is much higher that those for $Q \neq 0$. The heat release of combustion therefore reduces a_2, which would tend to increase the limiting scalar deviation, ΔZ, and the wrinkle length, d. This last tendency, however, tends to be offset by the influence of a_1 which, as shown before, decreases when $Q \neq 0$.

Conditional p.d.f.s for a_2 at $Z_s = 0.2$ are shown in figure 24. After scaling by the factor $1 + Q$, they do not vary much with Q, and they tend to have approximately exponential tails, being neither Gaussian nor log-normal. The factor $1 + Q$ helps because the singularity of the density at $Z = Z_s$ raises the peak of the p.d.f. Although there have been simulation-based studies of scalar fields and their gradients in non-premixed turbulence, Ashurst *et al.* (1987), p.d.f.s for second-derivative quantities like a_2 have been addressed through DNS only for premixed turbulent combustion (Shepherd & Ashurst 1992; Ashurst & Shepherd 1997); these last studies were focused on the curvature $\partial n_i / \partial x_i$ because of its influence on premixed flame-front propagation, but the general shapes of the resulting p.d.f.s are remarkably similar to figure 24. It would be of interest in the future to extract p.d.f.s of curvature from the present database to help explain the shapes seen in figures 21 and 22, which have smoother regions of smaller curvature extending towards the $Z = 0$ boundary with sharper points of higher curvature protruding towards the fuel side, possibly because of the shearing effects on the isoscalar surface in the shear layer.

In figure 24, it is interesting that the mode, while positive, is nearly at $a_2 = 0$, and there is an appreciable probability that a_2 is negative in all cases. The probability that $a_2 > 0$ is approximately 0.6, independent of Q. This means, according to (9.8), that $(\mathrm{d}\chi/\mathrm{d}Z)_{Z=Z_s}$ is negative nearly as often as it is positive for $Z_s = 0.2$ in these flows. Instantaneous profile shapes of the scalar dissipation in the laminar flamelet form of figure 15 thus are the exception rather than the rule. Instantaneous profiles of $\chi(Z)$ at these high Reynolds numbers therefore are highly irregular, with $(\mathrm{d}\chi/\mathrm{d}Z)_{Z=Z_s} = 0$ probably being a better approximation than any counterflow flamelet model. There is a greater probability for a_2 to be positive at smaller values of Z; for example, for $Z = 0.05$ it was found that this probability is about 0.9 for $Q = 0$ and about 0.7 for $Q \neq 0$, but even these values imply that a reasonable fraction of the realizations

FIGURE 25. Conditional p.d.f. of ΔZ at $Z = Z_s$ for different levels of heat release.

Case	Q	μ_Z	σ_Z	$(\Delta Z)_m$	$\overline{\Delta Z}$
A	0.0	-1.399	1.605	0.247	0.898
B	3.73	-1.999	1.452	0.135	0.388
C	7.46	-1.733	1.368	0.177	0.451

TABLE 5. Parameters of the conditional ΔZ p.d.f. fit to a log-normal distribution at $Z = Z_s$. Here $(\Delta Z)_m$ denotes the most probable value and $\overline{\Delta Z}$ the expected value of ΔZ, conditioned at $Z = Z_s$.

have $a_2 < 0$. More research therefore is needed in modelling $\chi(Z)$ in turbulent combustion.

Since the wrinkle length of (9.10) is non-negative by definition, it is reasonable to consider approximating its p.d.f. as log normal. Such an approximation does indeed work well for d, as it also does for ΔZ of (9.11). The latter agreement is demonstrated in figure 25. With

$$P(\Delta Z | Z_s) = \frac{1}{\sqrt{2\pi\sigma_Z^2}} \exp\left(-\frac{(\ln(\Delta Z) - \mu_Z)^2}{2\sigma_Z^2}\right), \qquad (9.12)$$

for $Z_s = 0.2$ the parameters μ_Z and σ_Z are listed in table 5, as are the mean $\overline{\Delta Z}$ and the mode $(\Delta Z)_m$ in the p.d.f. of ΔZ itself. It is seen that heat release greatly reduces the magnitude of the limiting scalar deviation at this Z_s and also decreases its variance somewhat, increasing the height of the peak of its p.d.f. This is a consequence of the associated decrease of $|\nabla Z|$, since in the identity $\Delta Z = |\nabla Z| d$, the wrinkle length d is actually increased somewhat by heat release at this Z_s, tending to slightly increase the range of applicability of flamelet concepts with increasing Q, a tendency which is offset by the decrease in $|\nabla Z|$. Comparing the ΔZ values in table 5 with the value of Z_s, namely 0.2, indicates that flamelet concepts are less applicable on average with heat release, although the decreasing variance may help to increase the fraction of realizations to which flamelet concepts apply. These changes with Q are results of the density reduction influencing the turbulence and are not associated with changes in viscosity or molecular diffusivities.
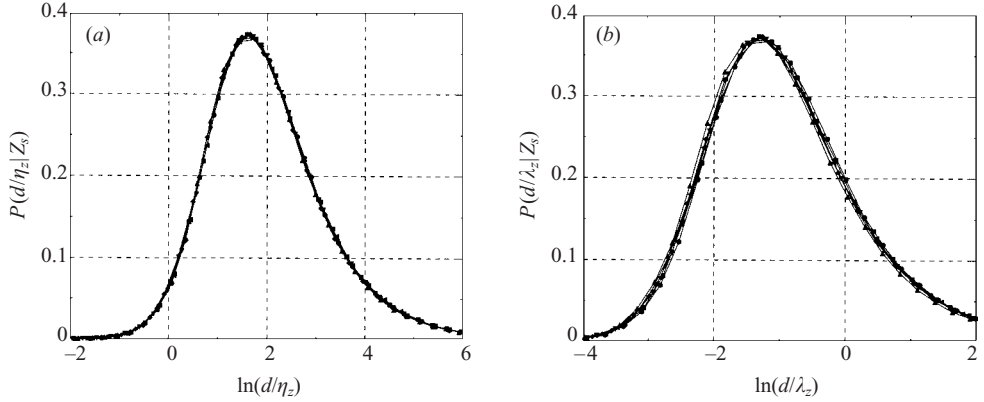
FIGURE 26. Conditional p.d.f. of d at $Z = Z_s$ for simulation B at a turbulence Reynolds number Re_t from about 400 to 600; the wrinkle length is normalized by (a) η_Z and (b) λ_Z.

Finally, it is of interest to consider how the statistics of the limiting scalar deviations ΔZ may scale with Reynolds number. If the wrinkle length d is of the order of the Taylor scale of the Z field, $\lambda_Z = \sqrt{D_s/\tilde{\chi}}$, then according to (9.11) ΔZ is independent of Reynolds number, since a_1 scales as $\sqrt{\tilde{\chi}/D_s}$. But if d instead is of the order of the Corrsin scale, $\eta_Z = (D_s^3/\tilde{\epsilon})^{1/4}$, as may be expected from its definition, then ΔZ scales as $Z_k/Sc^{1/4}$, where the order of magnitude of the scalar variations at the Kolmogorov scale, $Z_k = (\tilde{\chi}^2 v_s/\tilde{\epsilon})^{1/4}$, scales as $Re_t^{-1/4}$, the turbulence Reynolds number, proportional to Re_ω of (3.29), being defined here as $Re_t = \tilde{k}^2/(v_s \tilde{\epsilon})$. More precisely, from (6.1)–(6.3),

$$Z_k = \overline{Z''^2}^{1/2} r^{1/2}/Re_t^{1/4},$$

but the dominant scaling variation for ΔZ in this last result is the inverse fourth-root dependence on Reynolds number. Bilger (2000) asserts that the root-mean-square value of $4D_s|a_2|$ is approximately $3.5D_s \overline{a_1^2} Sc^{1/4}/Z_k$, equivalent to the scaling $Z_k/Sc^{1/4}$ for ΔZ, as can be seen from (9.11), and he points out the consequent inverse fourth-root dependence on Re_t. An attempt can be made to use the present DNS results to test these two different scaling hypotheses because Re_ω varies with time during the simulation, as previously indicated. Figure 26 shows p.d.f.s for the wrinkle length scaled with (a) η_Z and (b) λ_Z with data from simulation B at different times; conclusions from the other two simulations are similar. The curves collapse better with η_Z than with λ_Z, supporting Bilger's result. Corresponding curves employing δ_ω instead show much less agreement, indicating that the integral scale is certainly inappropriate, as expected. Although it clearly is most reasonable that η_Z is best, implying the $Re_t^{1/4}$ scaling for ΔZ, because of the small range of Re_t, the small power and possible effects of time evolution and initial conditions, the conclusions from the present simulations are not definitive in this respect.

10. Conclusions

The shear layer between two streams with relative velocity and exothermic chemical reaction is studied with DNS on grids with up to 40 million grid points. The chemical reaction of diluted methane with air is considered with a stoichiometric mixture fraction of $Z_s = 0.2$. The assumption of infinitely fast chemistry is made to obtain turbulent flow with reasonably large Reynolds number. The level of heat

release is varied from zero to full heat release, $T_f/T_o \simeq 7$, for the stoichiometry considered. The main objective of the current study is to evaluate the influence of heat release on the scalar field, in particular the mixing properties relevant to modelling flow/chemistry interaction in non-premixed turbulent combustion. Large computational domains, large computational grids, and broadband initial conditions ensure that the application of a high-order numerical scheme results in a simulated flow that corresponds to full-blown turbulence. The Reynolds number based on vorticity thickness is as large as 12 000.

It is shown that the effect of heat release on the profiles of unconditional scalar dissipation is minimized when the vorticity thickness, not the momentum thickness, is used as the characteristic length scale for normalization. In the shear layer, the peak values are characterized by $\chi_{peak} \simeq 0.012 \Delta u/\delta_\omega$.

The effect of heat release on the mixing properties of the shear layer is studied. Results are shown for the behaviour of the scalar p.d.f. and scalar dissipation conditioned on the scalar. It is shown that, unlike the constant-density case, the average scalar dissipation conditioned on the scalar depends strongly on the scalar value in the cases with heat release. These results have important implications for modelling purposes.

It is found that with heat release the scalar p.d.f. has a peak that is well correlated with the location of the expected value of the scalar, but without heat release the peak of the p.d.f. and the location of the mean value are poorly correlated. Furthermore, mean profiles of velocity and scalar differ for Reynolds and Favre forms by amounts that increase with increasing heat release. The effect is more pronounced on the scalar than on the velocity profiles because of the strong correlation between the density and the scalar.

The effect of heat release on the cross-stream profile of average reaction rate per unit volume is also studied. It is found that the peak reaction rate decreases with increasing heat release, and the profiles become narrower. The decrease is due to both the decrease of density and the change in scalar mixing with respect to passive scalar mixing.

A new random variable a_2, (9.3), relevant to variations of Z and χ in the vicinity of stoichiometric surfaces is defined, and its statistical properties are investigated. A wrinkle length is defined in terms of χ and a_2, representing the distance normal to a stoichiometric surface beyond which Z ceases to vary linearly with normal distance. This length increases with χ and also increases somewhat with heat release. The associated scalar deviation, however, is smaller with heat release, so that heat release may tend to reduce the applicability of flamelet models. Moreover, steady flamelet models are inapplicable for an appreciable fraction of the flamelets because, for example, there is a significant probability that $d\chi/dZ < 0$ for $Z < 0.5$, contrary to the laminar flamelet prediction that $d\chi/dZ > 0$ for $Z < 0.5$. Turbulence at high Reynolds number greatly distorts instantaneous $\chi(Z)$ profiles. Further study of the topology of isoscalar surfaces and of variations of Z and χ normal to these surfaces in flows with density changes typical of combustion may suggest improved descriptions of reaction zones at high Damköhler and Reynolds numbers in non-premixed turbulent combustion.

REFERENCES

ANSELMET, F. & ANTONIA, R. 1985 Joint statistics between temperature and its gradients in a turbulent jet. *Phys. Fluids* **28**, 1048–1054.

ASHURST, W., KERSTEIN, A., KERR, R. & GIBSON, C. 1987 Alignment of vorticity and scalar gradient with strain rate in simulated Navier–Stokes turbulence. *Phys. Fluids* **30**, 2343–2353.

ASHURST, W. & SHEPHERD, I. 1997 Flame front curvature distributions in a turbulent premixed flame zone. *Combust. Sci. Tech.* **124**, 115–144.

BALAKRISHNAN, G., SARKAR, S. & WILLIAMS, F. A. 1995 Direct numerical simulation of diffusion flames with large heat release in compressible homogeneous turbulence. *AIAA Paper* 95-2375.

BARLOW, R., FIECHTNER, G., CARTER, C. & CHEN, J. 2000 Experiments on the scalar structure of turbulent $CO/H_2/N_2$ jet flames. *Combust. Flame* **120**, 549–569.

BILGER, R. 1976a The structure of diffusion flames. *Combust. Sci. Tech.* **13**, 155–170.

BILGER, R. 1976b Turbulent jet diffusion flames. *Prog. Energy Combust. Sci.* **1**, 87–109.

BILGER, R. 1977 Comment on "structure of turbulent shear flows: A new look". *AIAA J.* **15**, 1056.

BILGER, R. 1980 *Turbulent Reacting Flows*, chap. 3. Springer.

BILGER, R. 2000 Future progress in turbulent combustion research. *Prog. Energy Combust. Sci.* **26**, 367–380.

BILGER, R. W. 1993 Conditional moment closure for turbulent reacting flow. *Phys. Fluids* **5**, 436–444.

BOGDANOFF, D. 1983 Compressibility effects in turbulent shear layers. *AIAA J.* **21**, 926–927.

DE BRUYN KOPS, S. & RILEY, J. 2000 Re-examining the thermal mixing layer with numerical simulations. *Phys. Fluids* **12**, 185–192.

BURKE, S. & SCHUMANN, T. 1928 Diffusion flames. *Proc. Combust. Inst.* **1**, 2–11.

CHEN, Y. & MANSOUR, M. 1997 Measurements of scalar dissipation in turbulent hydrogen diffusion flames and some implications on combustion modelling. *Combust. Sci. Tech.* **126**, 291–313.

CLEMENS, N. & PAUL, P. 1995 Scalar measurements in compressible axisymmetric mixing layers. *Phys. Fluids* **7**, 1071–1081.

CLEMENS, N. T. & MUNGAL, M. G. 1995 Large-scale structure and entrainment in the supersonic mixing layer. *J. Fluid Mech.* **284**, 171–216.

DAY, M., MANSOUR, N. & REYNOLDS, W. 2001 Nonlinear stability and structure of compressible reacting shear layers. *J. Fluid Mech.* **446**, 375–408.

ERLEBACHER, G., HUSSAINI, M., KREISS, H. & SARKAR, S. 1990 The analysis and simulation of compressible turbulence. *Theor. Comput. Fluid Dyn.* **2**, 73–95.

ESWARAN, V. & POPE, S. 1988 Direct numerical simulations of the turbulent mixing of a passive scalar. *Phys. Fluids* **31**, 506–520.

FIEDLER, H. 1974 Transport of heat across a plane turbulent mixing layer. *Adv. Geophys.* **18A**, 93–109.

GHARBI, A., RUFFIN, E., ANSELMET, F. & SCHIESTEL, R. 1996 Numerical modelling of variable density turbulent jets. *Intl J. Heat Mass Transfer* **39**, 1865–1882.

GIBSON, C. 1968 Fine structure of scalar fields mixed by turbulence. I. Zero-gradient points and minimal gradient surfaces. *Phys. Fluids* **11**, 2305–2315.

GIVI, P. 1989 Model-free simulations of turbulent reactive flows. *Prog. Energy Combust. Sci.* **15**, 1–107.

HERMANSON, J. & DIMOTAKIS, P. 1989 Effects of heat release in a turbulent, reacting shear layer. *J. Fluid Mech.* **199**, 333–375.

HIGUERA, F. & MOSER, R. 1994 Effect of chemical heat release in a temporally evolving mixing layer. *CTR Rep.*, pp. 19–40.

HIRAI, S. & TAKAGI, T. 1991 Numerical prediction of turbulent mixing in a variable-density swirling pipe flow. *Intl J. Heat Mass Transfer* **34**, 3143–3150.

JONES, W. 1994 *Turbulent Reacting Flows*, chap. 6. Academic.

JOU, W.-H. & RILEY, J. 1989 Progress in direct numerical simulations of turbulent reacting flows. *AIAA J.* **27**, 1543–1556.

JUNEJA, A. & POPE, S. 1996 A DNS study of turbulent mixing of two passive scalars. *Phys. Fluids* **8**, 2161–2184.

KENNEDY, I. & KENT, J. 1978 Measurements of a conserved scalar in turbulent jet diffusion flames. *Proc. Combust. Inst.* **17**, 279–287.

KERR, R. 1985 Higher-order derivative correlations and the alignment of small-scale structures in isotropic numerical turbulence. *J. Fluid Mech.* **153**, 31–58.

KERSTEIN, A. & ASHURST, W. 1984 Lognormality of gradients of diffusive scalars in homogeneous, two-dimensional mixing systems. *Phys. Fluids* **27**, 2819–2827.

KLIMENKO, A. 1990 Multicomponent diffusion of various admixtures in turbulent flow. *Fluid Dyn.* **25** (3), 3–10.

KOLLMANN, W. & JANICKA, J. 1982 The probability density function of a passive scalar in turbulent shear flows. *Phys. Fluids* **25**, 1755–1769.

LEE, Y. & POPE, S. 1995 Nonpremixed turbulent reacting flow near extinction. *Combust. Flame* **101**, 501–528.

LELE, S. 1992 Compact finite differences schemes with spectral-like resolution. *J. Comput. Phys.* **103**, 16–42.

LEONARD, A. & HILL, J. 1991 Scalar dissipation and mixing in turbulent reacting flows. *Phys. Fluids* A **3**, 1286–1299.

LI, J. & BILGER, R. 1993 Measurement and prediction of the conditional variance in a turbulent reactive-scalar mixing layer. *Phys. Fluids* A **5**, 3255–3264.

LIDE, D. (Ed.) 1999 *Handbook of Chemistry and Physics*. CRC Press.

LIVESCU, D., JABERI, F. & MADNIA, C. 2002 The effects of heat release on the energy exchange in reacting turbulent shear flow. *J. Fluid Mech.* **450**, 35–66.

MAHALINGAM, S., CHEN, J. & VERVISCH, L. 1995 Finite-rate chemistry and transient effects in direct numerical simulations of turbulent nonpremixed flames. *Combust. Flame* **102**, 285–297.

MCMURTRY, P., RILEY, J. & METCALFE, R. 1989 Effects of heat release on the large-scale structure in turbulent mixing layers. *J. Fluid Mech.* **199**, 297–332.

MELL, W. E., NILSEN, V., KOSÁLY, G. & RILEY, J. J. 1994 Investigation of closure models for nonpremixed turbulent reacting flows. *Phys. Fluids* **6**, 1331–1356.

MILLER, M., BOWMAN, C. & MUNGAL, M. 1998 An experimental investigation of the effects of compressibility on a turbulent reacting mixing layer. *J. Fluid Mech.* **356**, 25–64.

MILLER, R., MADNIA, C. & GIVI, P. 1994 Structure of a turbulent reacting mixing layer. *Combust. Sci. Tech.* **99**, 1–36.

MOIN, P. & MAHESH, K. 1998 Direct numerical simulation: A tool in turbulence research. *Annu. Rev. Fluid Mech.* **30**, 539–578.

MONTGOMERY, C., KOSÁLY, G. & RILEY, J. 1993 Direct numerical simulation of turbulent reacting flow using a reduced hydrogen–oxygen mechanism. *Combust. Flame* **95**, 247–260.

MONTGOMERY, C., KOSÁLY, G. & RILEY, J. 1997 Direct numerical solution of turbulent nonpremixed combustion with multistep hydrogen–oxygen kinetics. *Combust. Flame* **109**, 113–144.

MUNGAL, M. & DIMOTAKIS, P. 1984 Mixing and combustion with low heat release in a turbulent shear layer. *J. Fluid Mech.* **148**, 349–382.

NANDULA, S., BROWN, T., PITZ, R. & DEBARBER, P. 1994 Single-pulse, simultaneous multipoint multispecies Raman measurements in turbulent nonpremixed jet flames. *Opt. Lett.* **19**, 414–416.

NEWMAN, G., LAUNDER, B. & LUMLEY, J. 1981 Modelling the behaviour of homogeneous scalar turbulence. *J. Fluid Mech.* **111**, 217–232.

NOMURA, K. & ELGHOBASHI, S. 1992 Mixing characterisitcs of an inhomogeneous scalar in isotropic and homogeneous sheared turbulence. *Phys. Fluids* **4**, 606–625.

OVERHOLT, M. & POPE, S. 1996 Direct numerical simulation of a passive scalar with imposed mean gradient in isotropic turbulence. *Phys. Fluids* **8**, 3128–3148.

OVERHOLT, M. & POPE, S. 1999 Direct numerical simulation of a statistically stationary, turbulent reacting flow. *Combust. Theory Modelling* **3**, 371–408.

PANTANO, C. & SARKAR, S. 2002 A study of compressibility effects in the high-speed, turbulent shear layer using direct simulation. *J. Fluid Mech.* **451**, 329–371.

PAPAMOSCHOU, D. & ROSHKO, A. 1988 The compressible turbulent shear layer: an experimental study. *J. Fluid Mech.* **197**, 453–477.

PETERS, N. 1984 Laminar diffusion flamelet models in non-premixed models in turbulent combustion. *Prog. Energy Combust. Sci.* **10**, 319–339.

PETERS, N. 1986 Laminar flamelet concepts in turbulent combustion. *Proc. Combust. Inst.* **21**, 1231–1250.

PETERS, N. & TROUILLET, P. 2002 On the role of quasi-one-dimensional dissipation layers in turbulent scalar mixing. *Center for Turbulence, Stanford University, Annual Research Briefs*, pp. 27–40.

PLANCHÉ, O. 1992 A numerical investigation of the compressible reacting mixing layer. PhD thesis, Stanford University, Stanford, CA.

POPE, S. 1985 p.d.f. methods for turbulent reactive flows. *Prog. Energy Combust. Sci.* **11**, 119–192.

PUMIR, A. 1994 A numerical study of the mixing of a passive scalar in three dimensions in the presence of a mean gradient. *Phys. Fluids* **6**, 2118–2132.

RILEY, J., METCALFE, R. & ORSZAG, S. 1986 Direct numerical simulations of chemically reacting turbulent mixing layers. *Phys. Fluids* **29**, 406–422.

ROGERS, M. & MOSER, R. 1994 Direct simulation of a self-similar turbulent mixing layer. *Phys. Fluids* A **6**, 903–923.

SANCHEZ, A., LIÑÁN, A. & WILLIAMS, F. 1997 A generalized Burke–Schumann formulation for hydrogen–oxygen diffusion flames maintaining partial equilibrium of the shuffle reactions. *Combust. Sci. Tech.* **123**, 317–345.

SEPRI, P. 1976 Analysis of the pressure and velocity fields across steady diffusion flame sheets. *Combust. Flame* **26**, 179–189.

SHEPHERD, I. & ASHURST, W. 1992 Flame front geometry in premixed turbulent flames. *Proc. Combust. Inst.* **24**, 485.

SHIH, T. & LUMLEY, J. 1986 Influence of the time scale ratio on scalar flux relaxation: Modelling Sirivat and Warhaft's homogeneous passive scalar fluctuations. *J. Fluid Mech.* **162**, 211–222.

SHIH, T., LUMLEY, J. & JANICKA, J. 1987 Second order modelling of a variable density mixing layer. *J. Fluid Mech.* **180**, 93–116.

SHIN, D. & FERZIGER, J. 1991 Linear stability of the reacing mixing layer. *AIAA J.* **29**, 1634.

SPALDING, D. 1971 Concentration fluctuations in a round turbulent free jet. *Chem. Engng Sci.* **26**, 95–107.

STANLEY, S., SARKAR, S. & MELLADO, J. 2002 A study of the flow-field evolution and mixing in a planar turbulent jet using direct numerical simulation. *J. Fluid Mech.* **450**, 377–407.

STARNER, S., BILGER, R., LONG, M., FRANK, J. & MARRAN, D. 1997 Scalar dissipation measurements in turbulent jet diffusion flames of air diluted methane and hydrogen. *Combust. Sci. Tech.* **129**, 141–163.

SWAMINATHAN, N. & BILGER, R. 1997 Direct numerical simulation of turbulent nonpremixed hydrocarbon reaction zones using a two-step reduced mechanism. *Combust. Sci. Tech.* **127**, 167–196.

SWAMINATHAN, N., MAHALINGAM, S. & KERR, R. 1996 Structure of nonpremixed reaction zones in numerical isotropic turbulence. *Theor. Comput. Fluid Dyn.* **8**, 201–218.

TAVOULARIS, S. & CORRSIN, S. 1981 Experiments in nearly homogeneous turbulent shear flow with a uniform mean temperature gradient. Part I. *J. Fluid Mech.* **104**, 311–347.

THOMPSON, K. W. 1987 Time dependent boundary conditions for hyperbolic systems. *J. Comput. Phys.* **68**, 1–24.

VALIÑO, L., DOPAZO, C. & ROS, J. 1994 Quasistationary probability density functions in the turbulent mixing of a scalar field. *Phys. Rev. Lett.* **72**, 3518–3521.

VERVISCH, L. & POINSOT, T. 1998 Direct numerical heat release in the reacting turbulent plane shear layer. PhD thesis, The University of Adelaide; also *AFOSR Rep.* TR-84-0650. Simulation of non-premixed turbulent flames. *Annu. Rev. Fluid Mech.* **30**, 655–691.

WALLACE, A. 1981 Experimental investigation of the effects of chemical heat release in the reacting turbulent plane shear layer. PhD thesis, The University of Adelaide; also *AFOSR Rep.* TR-84-0650. Heat release in the reacting turbulent plane shear layer. PhD thesis, The University of Adelaide; also *AFOSR Rep.* TR-84-0650.

WARHAFT, Z. 2000 Passive scalars in turbulent flows. *Annu. Rev. Fluid Mech.* **26**, 211–254.

WILLIAMS, F. A. 1975 Recent advances in theoretical descriptions of turbulent diffusion flames. In *Turbulent Mixing in Non-reactive and Reactive Flows* (ed. S. Murthy), pp. 189–208. Plenum.

WILLIAMS, F. A. 1985 *Combustion Theory*. Benjamin/Cummings.

WILLIAMSON, J. 1980 Low-storage Runge–Kutta schemes. *J. Comput. Phys.* **35**, 48–56.